CMS Physics Analysis Summary

Contact: cms-pag-conveners-higgs@cern.ch 2020/07/30

Analysis of the CP structure of the Yukawa coupling between the Higgs boson and τ leptons in proton-proton collisions at $\sqrt{s} = 13$ TeV

The CMS Collaboration

Abstract

The first measurement of the CP structure of the Yukawa coupling between the Higgs boson and τ leptons is presented. The measurement is based on data collected in proton-proton collisions at $\sqrt{s} = 13$ TeV by the CMS experiment at the CERN LHC in 2016, 2017 and 2018, corresponding to an integrated luminosity of 137 fb^{-1}. Events are selected where one τ decays to a muon and the other hadronically, and where both τ leptons decay hadronically. These are the most sensitive decay modes for this analysis and together cover about 50% of all Higgs-to-tau decays. The analysis uses the angular correlation between the decay planes of τ leptons produced in Higgs boson decays. Machine learning techniques are deployed to distinguish between signal and background events, and dedicated analysis techniques are used to optimise the reconstruction of the τ decay planes. The mixing angle between CP-even and CP-odd τ Yukawa couplings was found to be $4 \pm 17^\circ$, compared to an expected uncertainty of $\pm 23^\circ$ at the 68% confidence level, while at the 95% confidence level the observed (expected) uncertainties were $\pm 36^\circ$ $(\pm 55)^\circ$. The observed (expected) significance of the separation between the CP-even and CP-odd hypotheses is 3.2 (2.3) standard deviations. The results are compatible with predictions for the standard model Higgs boson.

1 Introduction

In the standard model (SM) the electroweak symmetry breaking is postulated via the Brout–Englert–Higgs mechanism [1–3]. The mechanism predicts the existence of a scalar boson, the Higgs boson (H), which was discovered simultaneously by the ATLAS [4] and CMS [5] experiments at the CERN LHC using proton-proton (pp) collision data collected in 2011 and 2012 at centre-of-mass energies of 7 and 8 TeV, respectively. Since 2012 the coupling of the Higgs boson to τ leptons has been measured [6–8].

The SM Higgs boson is even under charge-parity (CP) inversion. Therefore, the CP structure of the couplings of the Higgs boson is an observable of outmost interest. A deviation from a purely scalar (CP-even, $J^{PC} = 0^{++}$) interaction in any coupling would be a direct indication of new physics.

The CMS and ATLAS Collaborations have studied the couplings of the Higgs boson to vector gauge bosons, including tests of CP violation [9–21], respectively. These studies excluded pure pseudoscalar couplings (CP-odd, $J^{PC} = 0^{-+}$) of the Higgs boson to gauge bosons.

CP violating effects are expected to be more experimentally accessible in Higgs boson's couplings to fermions than those to gauge bosons. In couplings to gauge bosons CP-odd contributions enter either via higher-order operators that are suppressed by powers of $1/\Lambda^2$ [22], where Λ is the scale of the new physics in an effective field theory, or via non-renormalisable interaction terms [23, 24]. Therefore these are expected to only yield a minor contribution to the coupling. A renormalisable CP-violating Higgs-to-fermion coupling may occur at tree level. The τ and top Yukawa couplings, H$\tau\tau$ and Htt respectively, are therefore the optimal couplings for CP studies in pp collisions [25], and measurements of these two couplings are complementary.

The H$\tau\tau$ coupling can be decomposed into a CP-even and a CP-odd coupling denoted as κ_τ and $\tilde{\kappa}_\tau$, respectively, via [25]:

$$\mathcal{L}_Y = -\frac{m_\tau \mathrm{H}}{\mathrm{v}}(\kappa_\tau \bar{\tau}\tau + \tilde{\kappa}_\tau \bar{\tau} i\gamma_5 \tau). \tag{1}$$

In this equation m_τ is the mass of the τ lepton, and the vacuum expectation value, v, has a value of 246 GeV. The effective mixing angle $\phi_{\tau\tau}$ for the H$\tau\tau$ coupling is defined in terms of the couplings as

$$\tan(\phi_{\tau\tau}) = \frac{\tilde{\kappa}_\tau}{\kappa_\tau}, \tag{2}$$

while the fractional contribution of the CP-odd coupling $f_{\mathrm{CP}}^{\tau\tau}$ is obtained from the mixing angle as $f_{\mathrm{CP}}^{\tau\tau} = \sin^2(\phi_{\tau\tau})$. The effective mixing angle in the Htt coupling is defined equivalently as ϕ_{tt}. A mixing angle of $\phi_{\tau\tau}$ =0 $(90)^\circ$ corresponds to a pure scalar (pseudoscalar) coupling. For any other value of $\phi_{\tau\tau}$ the Higgs boson has a mixed coupling with CP-even and CP-odd components, with maximal mixing at a value of 45°.

Recently, both the CMS [26] and ATLAS [27] Collaborations presented first measurements of the CP structure of the Higgs coupling to top quarks. The CMS results rejected the purely CP-odd hypothesis with a significance of 3.2 standard deviations, while the ATLAS analysis rejected this hypothesis with a significance of 3.9 standard deviations. The two experiments measured an observed (expected) uncertainty on the mixing angle at 95% CL of 55 $(65)^\circ$ and 43 $(63)^\circ$, respectively. Both measurements yielded values consistent with SM predictions.

The measurement of a nonzero mixing angle would have implications for certain new physics models, such as supersymmetric models and 2HDM [28]. For example, in the minimal supersymmetric model, CP violation in the Higgs-to-fermion couplings is small. In the next-to-minimal supersymmetric model $\phi_{\tau\tau}$ can be larger but is not allowed to exceed $\approx 27^\circ$. These upper bounds originate from exclusion limits, the currently known Higgs parameters, and constraints on the electric dipole moment of the electron and muon [29].

This is the first analysis that directly measures the potential mixing between a scalar and pseudoscalar $H\tau\tau$ coupling. This is performed by measuring the angles between the τ decay planes, which has the advantage that it is a model-independent measurement. The precision to which $\phi_{\tau\tau}$ can be measured by an LHC experiment with 150 (500) fb^{-1} of proton-proton collisions has been estimated to be 27° (14°) at the 68% confidence level [30]. Also the ATLAS Collaboration has performed a Phase 2 projection study, limited to the $\tau^\pm \to \rho^\pm\nu \to \pi^\pm\pi^0\nu$ channel [31].

The decay of a (pseudo) scalar Higgs boson into two fermions can be written as [32, 33]

$$\Gamma(\mathrm{H} \to f\bar{f}) \propto 1 - s_z\bar{s}_z \pm C s_\perp \bar{s}_\perp, \tag{3}$$

in which s and $\bar{s}$ are the spin vectors of the τ leptons in the τ rest frames, and C is a unitary complex number. The transverse part in the equation enters with a real and positive (negative) sign if H is a scalar (pseudoscalar). For mixed couplings C takes a complex value.

The transverse spin components of the τ affect the angular correlation of the di-τ decay products. For τ decays to a charged pion and neutrino the transverse momentum components of the charged pions are predominantly anti-aligned for a scalar decay, and aligned instead for a pseudoscalar. Consequently, the angle between the decay planes of the τ leptons is sensitive to $\phi_{\tau\tau}$; the relation between the τ decay plane and its decay products is discussed in Section 2.

This analysis uses the $137\,\text{fb}^{-1}$ data set of pp collisions at $\sqrt{s} = 13\,\text{TeV}$ collected with the CMS experiment at the LHC in 2016, 2017, and 2018. We denote a τ decaying to hadrons as τ_h, and a τ decaying to a muon as τ_μ. The sign of the τ leptons is only indicated when relevant for the τ decay chain. This analysis targets the $\tau_\text{h}\tau_\text{h}$ and $\tau_\mu\tau_\text{h}$ decay channels, which are the most sensitive for the analysis. This covers about 50% of all possible di-τ final states.

2 Analysis strategy

In this section we present the different methods that are used in the analysis to reconstruct the τ decay planes and outline the strategy to optimise the signal sensitivity. We define ϕ_CP as the angle between the τ decay planes. In Fig. 1 we show the ϕ_CP distributions, calculated in the rest frame of the boson, for the scalar, pseudoscalar, and maximally mixed values of $\phi_{\tau\tau}$, as well as the ϕ_CP distribution from Drell-Yan processes. These distributions are for both τ leptons decaying to a charged pion and a neutrino.

There is a phase shift between different mixing scenarios such that the difference in ϕ_CP equals $2\phi_{\tau\tau}$. It is important to note that the distribution of ϕ_CP of a decaying vector boson is flat; we will exploit this symmetry as explained in section 8.

The observable ϕ_CP was originally introduced in e^+e^- collisions [32, 34] where the τ momentum can be reconstructed. In hadronic collisions the momenta of the neutrinos cannot be well constrained and so methods of estimating ϕ_CP have been extended and optimised for hadronic collisions [30].

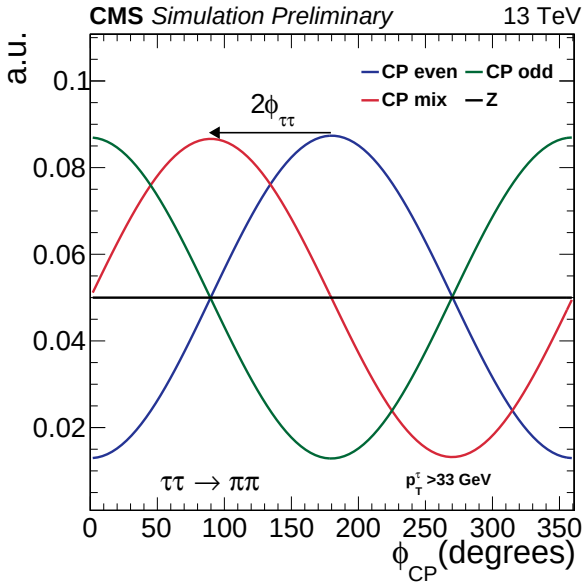

Figure 1: The normalised distribution of ϕ_{CP} between the τ decay planes in the boson rest frame, for both τ leptons decaying to a charged pion and a neutrino. The distributions are for a decaying scalar (CP even, blue), pseudoscalar (CP odd, green), a maximal mixing angle of 45° (CP mix, red), and a Z vector boson (black). A p_T cutoff of 33 GeV is applied on the visible τ decay products.

Table 1 summarises the τ decay modes used in this analysis, their branching fractions, and the shorthand symbol that we use to denote them in the rest of this paper. Various methods can be used to reconstruct the decay planes $\lambda^\pm$ of the $\tau^\pm$ leptons depending on the τ topology and these are described below.

Table 1: Weak decays of τ leptons used in this analysis and their branching fractions $\mathcal{B}$ in % [35] are given, rounded to one decimal place. Also, where appropriate, we indicate the known intermediate resonances of all the hadrons listed. The muon is accompanied by two neutrinos, while the hadronic modes involve one neutrino. The third row gives the shorthand notation for the decays used throughout this note.

Mode	$\mu^\pm$	$\pi^\pm$	$\rho^\pm \rightarrow \pi^\pm\pi^0$	$a_1{}^\pm \rightarrow \pi^\pm\pi^0\pi^0$	$a_1{}^\pm \rightarrow \pi^\pm\pi^\mp\pi^\pm$
$\mathcal{B}(\%)$	17.4	11.5	25.9	9.5	9.8
Symbol	μ	π	ρ	a_1^{1pr}	a_1^{3pr}

2.1 Impact parameter method

The impact parameter method exploits the finite lifetime of the τ lepton. We define the impact parameter $\mathbf{j}^\pm$ as the vector between the primary vertex (PV) and the point of closest approach (PCA) of the track of the charged particle. The PCA is defined as the point on the track where the distance between the track and primary vertex is minimal (a further explanation on the extraction of the impact parameters is provided in Section 5). Thus, the impact parameter is an experimental observable.

We define the decay plane $\boldsymbol{\lambda}^\pm$ as the plane spanned by the impact parameter vector and the charged particle vector. This plane only represents the genuine plane of the decay into a single charged pion and neutrino in the rest frame of the Higgs boson when boosted into that frame. However, in pp interactions this frame can only be estimated with large uncertainties when the Higgs boson decays to τ leptons and so we use the charged products of the Higgs boson

decays to define a zero-momentum frame (ZMF) into which $\boldsymbol{\lambda}^{\pm}$ are boosted. This means that this method does not reconstruct the genuine τ decay plane, but rather a plane that is correlated to it.

We construct a 4-component vector in the laboratory frame as $\lambda^{\pm} = (0, \mathbf{j}^{\pm})$. These four vectors $\lambda^{\pm}$ are boosted in the ZMF and denoted $\lambda^{*\pm}$. We also boost the respective charged pion four vectors to the ZMF, denoted $q^{*\pm}$. Then we take the transverse components of $\lambda^{*\pm}$ w.r.t. $q^{*\pm}$. We normalise the vectors to obtain unit vectors $\hat{\lambda}^{*+}_{\perp}$ and $\hat{\lambda}^{*-}_{\perp}$. From these vectors we reconstruct the angles ϕ^* and O^* as:

$$\begin{aligned} \phi^* &= \arccos(\hat{\lambda}^{*+}_{\perp} \cdot \hat{\lambda}^{*-}_{\perp}) \\ O^* &= \hat{q}^{*-} \cdot (\hat{\lambda}^{*+}_{\perp} \times \hat{\lambda}^{*-}_{\perp}), \end{aligned} \tag{4}$$

From ϕ^* and O^* we reconstruct ϕ_{CP} on a range $[0, 360^\circ]$ as:

$$\phi_{\mathrm{CP}} = \begin{cases} \phi^* & \text{if } O^* \geq 0 \\ 360^\circ - \phi^* & \text{if } O^* < 0 \end{cases} \tag{5}$$

The decay planes for the impact parameter method are illustrated in Fig. 2 (left). We note that a phase flip occurs in ϕ_{CP} for leptonic decays because of the opposite sign in the τ spectral functions [36].

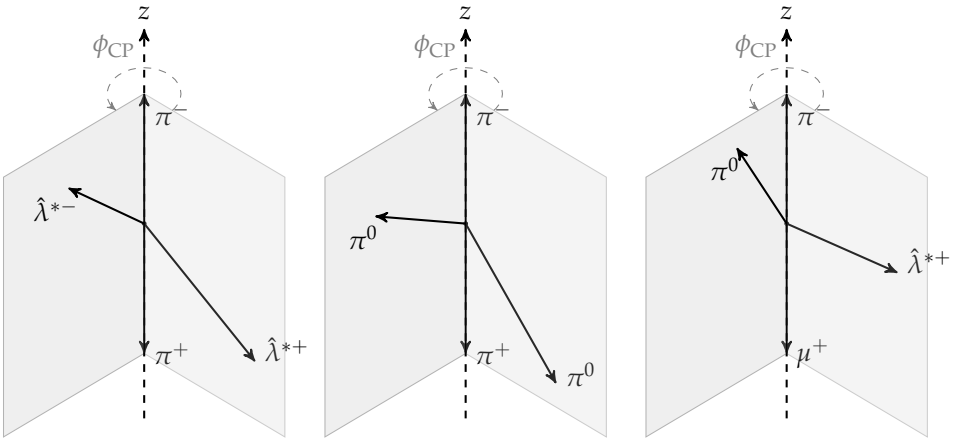

Figure 2: Left: illustration of the decay plane for the decay $\tau^- \to \pi^- + \nu$. Middle: illustration of the decay plane as reconstructed from the neutral and charged pion momentum. Right: illustration of ϕ_{CP} for the mixed scenario, in which one τ lepton decays to a single charged pion while the other decays via an intermediate ρ meson. The illustrations are in the zero-momentum frame of the charged particles.

2.2 Neutral pion method

The neutral pion method can be applied to hadronic decay channels involving more than one outgoing hadron. We describe the method applied to the intermediate $\rho(770)$ decay, the intermediate $a_1(1260)$ to 1-prong decay [37, 38], and the 3-prong decay modes.

An advantage of the neutral pion method is that it does not rely on the reconstruction of the impact parameter. The τ impact parameter is relatively small compared to the tracking resolution and the fine granularity of the CMS electromagnetic calorimeter means that the direction of neutral pions can be reconstructed with smaller relative uncertainties.

For the ρ decays the vector λ is replaced by the four-momentum vector of the π^0. The method is applied to a_1^{1pr} decays involving two neutral pions by summing the neutral constituents in the decay. The angle ϕ_{CP} is then calculated in an analogous method to that used in the impact parameter method except that to avoid destructive interference from differently polarised states of the mesons, the following observables need to be defined:

$$y^{\tau^\pm} = \frac{E_{\pi^\pm} - E_{\pi^0}}{E_{\pi^\pm} + E_{\pi^0}}, \quad y^\tau = y^{\tau^-} y^{\tau^+}, \tag{6}$$

in which E_π is the energy of the pion in the laboratory frame. If y^τ is negative, ϕ_{CP} is obtained via the shift $360^\circ - \phi_{CP}$. The decay plane and its relation to ϕ_{CP} is graphically illustrated in Fig. 2 (middle).

The neutral pion method can also be successfully adapted to the a_1^{3pr} decay mode. Here we select the oppositely charged pion pair with an invariant mass closest to a ρ^0. Of this pair we treat the pion with charge opposite to that of the τ as though it was a π^0, and the momentum of the pion with same sign as the τ is used for the calculation of the ZMF. After these assignments the neutral pion method is applied as described for 1-prong decays.

2.3 Strategy

The short lifetime of the τ and the finite resolution of the tracking system when reconstructing both the PV and the charged tracks means that, although the impact parameter method can in principle be applied to every τ decay mode, in this analysis we only use the impact parameter for the π and μ decays, while for the other modes the neutral pion method is used instead.

Where one τ decays to a single hadron or charged lepton and the other to multiple hadrons a mixture of the two methods is used, as illustrated in Fig. 2 (right).

Both the finite resolution of the tracking and the misidentification of τ decay modes are of major importance to this analysis and we have developed dedicated approaches to mitigate their effects. These are described in Section 5, while the event categorisation to distinguish signal from background events is outlined in Section 8.

3 The CMS detector

From the central interaction point, the CMS detector hosts a silicon pixel and strip tracker, a lead tungstate crystal electromagnetic calorimeter (ECAL), and a brass and scintillator hadron calorimeter (HCAL), each composed of a barrel and two endcap sections. The central feature of the CMS apparatus is a superconducting solenoid of 6 m internal diameter, providing a magnetic field of 3.8 T. The silicon pixel and tracking systems as well as the calorimeters are contained within the solenoid volume. Muons are detected in gas-ionization chambers embedded in the steel flux-return yoke outside the solenoid.

The nominal pp bunch crossing rate at the LHC is 40 MHz. In order to reduce the rate of events that are recorded for offline analysis, events of interest are selected using a two-tiered trigger system [39]. The first level (L1) is composed of custom built electronics which makes use of high speed optical links and large Field Programmable Gate Arrays (FPGAs). L1 reduces the event rate from the nominal bunch crossing to a rate of around 100 kHz within a time interval of less than 3.5 μs. The second level, known as the High Level Trigger (HLT), consists of a farm of generic processors running a version of the full event reconstruction software that has been optimised for fast processing. It reduces the event rate to about 1 kHz before data storage.

This analysis has benefited from significant upgrades of the L1 trigger that have been implemented for the LHC pp collisions at $\sqrt{s} = 13\,\text{TeV}$, especially in the $\tau_\text{h}\tau_\text{h}$ channel. These upgrades improved the τ_h lepton identification at L1 by giving more flexibility to object isolation, allowing new techniques to suppress the contribution from additional pp interactions per bunch crossing, and to reconstruct the L1 τ_h object in a fiducial region that matches more closely that of a true hadronic τ decay.

A more detailed description of the CMS detector, together with a definition of the coordinate system used and the relevant kinematic variables, can be found in Ref. [40].

4 Data sets and simulated samples

This analysis uses the full pp data sets collected by the CMS experiment at $\sqrt{s} = 13\,\text{TeV}$ in 2016, 2017 and 2018. These correspond to integrated luminosities of 35.9, 41.5, and 59.7 fb^{-1} respectively. The signal and relevant background processes are modelled with samples of Monte Carlo simulated events.

The signal samples with a Higgs boson produced through gluon–gluon fusion (ggH), vector boson fusion (VBF), or in association with a W or Z vector boson (denoted as WH or ZH, or VH when combined), are generated at next-to-leading order (NLO) in perturbative quantum chromodynamics (pQCD) with the POWHEG 2.0 [41–45] event generator. The Higgs boson production mechanism is configured to only produce scalar Higgs bosons. The p_T spectrum of the Higgs boson is tuned in the POWHEG simulation of the gluon–gluon fusion production mode to better match predictions from full phase space calculations implemented in the HRES 2.3 generator [46, 47]. The decay of the Higgs boson does not depend on its production. The description of the decay of the Higgs boson to τ leptons is obtained using the PYTHIA generator version 8.2 [48, 49]. These samples are simulated without accounting for the τ spin correlations. After the samples have been generated, the TAUSPINNER package [50] is used to calculate event weights that can be applied to the simulated signal samples to model τ polarisation effects for a boson with CP-mixing angles of 0, 45°, and 90°. The average of these event weights is normalised to one, i.e. the integrated $\text{H} \to \tau\tau$ cross section of the signal samples is invariant under rotations in $\phi_{\tau\tau}$. All 2016 samples are generated with the NNPDF3.0 NLO parton distribution functions (PDFs), while for 2017 and 2018 the NNPDF3.1 distributions are used. The Higgs mass is fixed to 125 GeV.

The MG5_aMC@NLO [51] generator is used for processes involving a Z or W boson and a quark or gluon initiated jet, and these processes are denoted $\text{Z} + \text{jets}$ and $\text{W} + \text{jets}$, respectively. They are simulated at leading order (LO) with the MLM jet matching and merging [52]. The same generator is used for diboson production, whereas POWHEG 2.0 and 1.0 are used for top antitop quark pair ($\text{t}\bar{\text{t}}$) and single top quark production, respectively. The generators are interfaced with PYTHIA 8.2 to model the parton showering and fragmentation, as well as the decay of the τ leptons. The PYTHIA parameters that affect the description of the underlying event are set to the CUETP8M1 tune in 2016, and CP5 tune in 2017 and 2018 [53].

Monte Carlo generated events are processed through a simulation of the CMS detector which is based on GEANT4 [54], and are reconstructed with the same algorithms as used for data. Additional pp interactions per bunch crossing ("pileup") are included. The effect of pileup is taken into account by generating concurrent minimum bias collision events with PYTHIA. The pileup distribution in simulation is weighted to match the pileup in data.

5 Event reconstruction

The reconstruction algorithms of both observed and simulated events is based on the particle-flow (PF) algorithm [55], which relies on the information from the different CMS subdetectors to reconstruct muons, electrons, photons, and charged and neutral hadrons. These objects are combined to form more complex ones, like τ_h candidates or missing transverse momentum.

Muons are identified and reconstructed with requirements on the quality of the track reconstruction and on the number of hits in the tracker and muon systems [56]. Muons are selected with $|\eta| < 2.4$. In order to reject muons which originate from non-prompt interactions, or are misidentified, a relative muons isolation is defined:

$$I^{\ell} \equiv \frac{\sum_{\text{charged}} p_T + \max\left(0, \sum_{\text{neutral}} p_T - \frac{1}{2}\sum_{\text{charged, PU}} p_T\right)}{p_T^{\ell}}. \quad (7)$$

In this equation, $\sum_{\text{charged}} p_T$ is the scalar sum of the transverse momenta of the charged particles originating from the PV and located in a cone of size $\Delta R = \sqrt{(\Delta\eta)^2 + (\Delta\phi)^2} = 0.4$ centred on the muon direction. The sum $\sum_{\text{neutral}} p_T$ is a similar quantity for neutral particles, while $\sum_{\text{charged, PU}} p_T$ is a similar quantity for particles originating from pileup vertices. The p_T of the lepton is denoted by p_T^{ℓ}.

Electrons are reconstructed using tracks from the tracking system, calorimeter deposits in the ECAL and a veto on objects with a large HCAL to ECAL energy ratio. Electrons are identified using a multivariate (MVA) discriminant combining several quantities that describe the shape of the energy deposits in the ECAL, the quality of tracks, and the compatibility of the measurements from the tracker and the ECAL [57].

Jets are reconstructed using the anti-k_T FASTJET algorithm [58] with distance parameter $R = 0.4$. The anti-k_T FASTJET algorithm functions by taking PF objects and grouping them together based on inverse powers of the object's transverse momentum [58, 59]. Data collected in the ECAL endcaps were affected by large amounts of noise during the 2017 run, which led to disagreements between simulation and data. To mitigate this issue, jets used in the analysis of the 2017 data are discarded if they have $p_T < 50\,\text{GeV}$ and $2.65 < |\eta| < 3.139$. Hadronic jets that contain b quarks are tagged using a Deep Neural Network (DNN), called the DeepCSV algorithm [60].

All particles reconstructed in the event are used to determine the missing transverse momentum, $\vec{p}_T^{\,\text{miss}}$. The missing transverse momentum is defined as the negative vectorial sum of the transverse momenta of all PF candidates and reconstructed using the PUPPI p_T^{miss} algorithm [61].

The reconstruction of τ_h leptons is performed with the Hadron-Plus-Strip (HPS) algorithm [62]. The algorithm works by combining the signature of charged hadrons, tracks left in tracker and energy deposits in the hadronic calorimeter, with the electron/photon signature of neutral pions reconstructed by collecting energy inside of "strips" in $\Delta\eta \times \Delta\phi$ space inside of the electromagnetic calorimeter. The combination of these signatures provides the four vector of the visible decay products of the parent τ_h. The identification of τ_h candidates makes use of isolation discriminators to reject quark and gluon jets that could be misidentified as τ_h. For this analysis, a DNN called DeepTau [63], is used on the HPS τ_h candidates to provide further discrimination. In order to achieve an optimal τ identification performance, the DNN combines information from the high-level reconstructed τ features together with the low-level information from the inner tracker, calorimeters and muon sub-detectors using PF candidates,

electrons and muons reconstructed within the τ_h isolation cone. The working point on the output discriminant is chosen to provide a τ_h ID and reconstruction efficiency of about 60% at a jet misidentification rate of approximately 5×10^{-3}. Two other DNNs are used to reject electrons and muons misidentified as τ_h candidates using dedicated criteria based on the consistency between the measurements in the tracker, the calorimeters, and the muon detectors.

The mass of the di-τ system, $m_{\tau\tau}$, is calculated using a simplified matrix-element algorithm, SVFIT [63], which combines the $\vec{p}_T^{\,\text{miss}}$ and its uncertainty matrix with the four-vectors of both τ candidates to calculate the mass of the parent boson. The resolution of $m_{\tau\tau}$ is between 15 and 20% depending on the $\tau\tau$ final state and the boost of the di-τ system.

5.1 Multivariate discriminant for τ decay mode identification

In Section 2 the different methods used to reconstruct ϕ_{CP} for different decay modes were described. In order to optimally discriminate between the different decay modes, we developed an MVA discriminant. It uses a boosted decision tree (BDT) algorithm combined with the XGBoost library [64], and is applied on top of the τ_h selection. The algorithm was trained to distinguish between the one and three-prong τ lepton decays: π, ρ, a_1^{1pr}, a_1^{3pr}, and $\pi^\pm\pi^\mp\pi^\pm\pi^0$. The $\pi^\pm\pi^\mp\pi^\pm\pi^0$ is not used in the extraction of the CP angle but must be separated from a_1^{3pr} to avoid contamination.

The inputs to the BDT are the kinematic features of the HPS τ and its constituents. The BDT exploits angular correlations between the decay products, invariant mass quantities, and kinematic properties of the photons.

5.2 Primary vertex reconstruction

The positions of all pp interactions (vertices) in the event, including the hard-scatter (primary vertex) and soft (pileup) ones, are reconstructed in a two-step procedure [65]. The steps consist of clustering the tracks that appear to originate from the same interaction using the Deterministic Annealing algorithm [66], and subsequently fitting the position of each vertex using tracks associated to its cluster with the Adaptive Vertex Fitter (AVF) algorithm [67]. The candidate vertex with the largest value of $\sum p_T^2$ of physics objects is considered to be the primary pp interaction vertex. The finite lifetime of the τ lepton means that tracks emanating from its decay do not originate from the PV. Within this analysis these tracks are removed and the PV is refitted using the remaining tracks as input to the AVF algorithm.

The LHC beamspot represents a 3-dimensional profile of the luminous region, where the LHC beams collide in the CMS detector. The parameters of the beamspot are determined from an average over many events [65]. The uncertainties in the beamspot parameters are relatively small and so it is incorporated into the AVF algorithm. The inclusion of the beamspot leads to an improvement of the PV resolution in the transverse plane of a factor $\mathcal{O}(3)$, while the z coordinate of the PV is largely unaffected. The refitted beamspot-corrected primary vertex is used throughout the analysis.

5.3 Impact parameter estimate and significance

A dedicated algorithm was developed to derive the impact parameter of the charged track from the τ lepton decay using a helical extrapolation of the track parameters.

This procedure has two advantages. Firstly, with this extrapolation the minimisation of the impact parameter is performed in three dimensions. For tracks with large pseudorapidity values,

the procedure leads to a better estimation of the z coordinate of the impact parameters than when the minimisation is done exclusively in the transverse plane.

Secondly, this helical extrapolation allows the propagation of both the track and PV uncertainties into an overall impact parameter significance S_{IP} (defined as the ratio of the magnitude of the impact parameter divided by its uncertainty). Events with a low S_{IP} would dilute the sensitivity of this analysis and so we discard events where the muon or pion track has $S_{\mathrm{IP}} < 1.5\sigma_{S_{\mathrm{IP}}}$.

6 Event selection

Events are selected online by the CMS trigger system. For the $\tau_\mu\tau_\mathrm{h}$ channel events are triggered by either a paired $\mu + \tau_\mathrm{h}$ cross trigger or a single-μ trigger with a higher p_T threshold for the μ compared to the cross trigger. For the $\tau_\mathrm{h}\tau_\mathrm{h}$ channel a di-τ trigger is used.

Offline, a pair of oppositely charged τ leptons separated by $\Delta R > 0.5$ is required. The offline reconstructed objects are required to match the trigger objects within a cone of $R = 0.5$. The offline reconstructed μ is required to have a p_T value that is at least 1 GeV higher than the online threshold. If an offline τ_h is matched to a τ_h trigger object (including the τ_h leg of the $\mu + \tau_\mathrm{h}$ cross trigger for the $\tau_\mu\tau_\mathrm{h}$ channel), the τ_h must have a p_T at least 5 GeV above the trigger threshold. If, in the $\tau_\mu\tau_\mathrm{h}$ channel, the event is selected online by the single-μ trigger the offline τ_h is required to have $|\eta| < 2.3$ and a p_T of at least 20 GeV.

Table 2 summarises the online trigger and offline p_T thresholds, μ isolation requirement, τ_h identification algorithm, and η acceptances for the $\tau_\mu\tau_\mathrm{h}$ and $\tau_\mathrm{h}\tau_\mathrm{h}$ channel for 2016, 2017, and 2018.

Table 2: Kinematic trigger and offline requirements applied for the $\tau_\mu\tau_\mathrm{h}$ and $\tau_\mathrm{h}\tau_\mathrm{h}$ channel. The trigger p_T requirement is indicated in parentheses (in GeV). The pseudorapidity constraints originate from trigger and reconstruction requirements.

Channel	year	Trigger requirement	Offline lepton selection		
			p_T (GeV)	η	Isolation
$\tau_\mathrm{h}\tau_\mathrm{h}$	all years	$\tau_\mathrm{h}(35)$ & $\tau_\mathrm{h}(35)$	$p_\mathrm{T}^{\tau_\mathrm{h}} > 40$	$\lvert\eta^{\tau_\mathrm{h}}\rvert < 2.1$	DNN τ_h ID
$\tau_\mu\tau_\mathrm{h}$	2016	$\mu(22)$, $\mu(19)$ & $\tau_\mathrm{h}(20)$	$p_\mathrm{T}^{\mu} > 20$	$\lvert\eta^{\mu}\rvert < 2.1$	$I^{\mu} < 0.15$
			$p_\mathrm{T}^{\tau_\mathrm{h}} > 25$	$\lvert\eta^{\tau_\mathrm{h}}\rvert < 2.3$	DNN τ_h ID
	2017, 2018	$\mu(24)$, $\mu(20)$ & $\tau_\mathrm{h}(27)$	$p_\mathrm{T}^{\mu} > 21$	$\lvert\eta^{\mu}\rvert < 2.1$	$I^{\mu} < 0.15$
			$p_\mathrm{T}^{\tau_\mathrm{h}} > 32$	$\lvert\eta^{\tau_\mathrm{h}}\rvert < 2.3$	DNN τ_h ID

For the $\tau_\mu\tau_\mathrm{h}$ channel, the large W+jets background is reduced by cutting on the transverse mass m_T of the μ:

$$m_\mathrm{T} \equiv \sqrt{2p_\mathrm{T}^{\mu}p_\mathrm{T}^{\mathrm{miss}}[1-\cos(\Delta\phi)]} < 50\,\mathrm{GeV}, \tag{8}$$

where $\Delta\phi$ is the azimuthal angle between the direction of the μ and $p_\mathrm{T}^{\mathrm{miss}}$.

The longitudinal and transverse impact parameters d_z and d_xy of the μ are required to satisfy $|d_\mathrm{z}| < 0.2\,\mathrm{cm}$ and $|d_\mathrm{xy}| < 0.045\,\mathrm{cm}$. These impact parameters originate from a minimisation of the magnitude of the impact parameters in the transverse plane only, in contrast with the impact parameters used for calculating ϕ_{CP} that are derived using a 3-dimensional minimisation. For the leading τ_h track only the requirement $|d_\mathrm{z}| < 0.2\,\mathrm{cm}$ is imposed. Further, a veto on events containing loosely identified additional electrons or muons is implemented. For the $\tau_\mu\tau_\mathrm{h}$ channel a veto on jets passing b-tagging requirements is used as well. When multiple τ

lepton pairs are present, the most isolated pair is chosen. The selection procedure is identical for data and simulated events.

7 Background estimation

The processes that contribute to the background in this analysis are Drell-Yan Z, W + jets, $t\bar{t}$, single top, and diboson production. Additionally, SM events comprised uniquely of jets produced through the strong interaction, referred to as quantum chromodynamics (QCD) multijet events, form a significant background. These processes contribute to the production of two genuine τ leptons, jets and leptons that are misidentified as τ_h, as well as prompt leptons that are misidentified as τ_μ in the $\tau_\mu\tau_h$ channel. All background processes resulting in two genuine τ leptons are the dominant (sub-leading) background for the $\tau_\mu\tau_h$ ($\tau_h\tau_h$) channel. These are estimated from data using a τ-embedding technique [68]. Events in which a jet is misidentified as a τ_h are the dominant (sub-leading) background in the $\tau_h\tau_h$ ($\tau_\mu\tau_h$) channel. The rates of misidentified jets for all processes are obtained via the derivation of fake factors in dedicated control regions in data. A detailed description is presented in [69]. In this section we succinctly outline the data-driven methods used to obtain the genuine di-τ and jet-misidentification backgrounds. Other smaller backgrounds are determined using simulated events.

7.1 Tau lepton embedding

In order to obtain the genuine di-τ background we exploit lepton universality, and replace di-μ pairs in data events with simulated di-τ pairs. The dominant process for this background is $Z \to \tau\tau$, but there are also small contributions from $t\bar{t}$ and diboson processes.

All events with an oppositely charged di-μ pair are collected. The detector hits belonging to the muon tracks are removed from these events. A Z boson is simulated, which is forced to decay to a di-τ pair with identical kinematics to the muon pair that was removed. The di-τ pair is forced to decay fully hadronically or semileptonically in order to simulate either the $\tau_h\tau_h$ or $\tau_\mu\tau_h$ channel. The detector response to the di-τ pair is then simulated and added to the data event. A detailed description may be found in [68].

7.2 The fake factor method

The fake factor method is designed to provide a data-driven estimate of the rate of all events in which at least one quark or gluon jet is misidentified as a τ_h lepton, and we refer to such a jet as a jet-fake.

We define a determination region that is orthogonal to the signal region and dominated by a background process resulting in jet-fakes. In this region we determine the ratio between the nominal-isolated τ_h rate (which are jet-fakes in this region) and the anti-isolated τ_h rate. This is achieved by demanding that the τ_h candidates fulfil a very loose isolation requirement, but fail the nominal τ isolation criterium (as described in Section 5.1). The ratio in the determination region is the fake factor. To obtain the rate of fake jets in the signal region, an application region is defined by selecting events that fulfil the event selection criteria except that they contain an anti-isolated τ_h lepton (for the $\tau_h\tau_h$ channel it must be the leading τ_h). The rate of fake jet events in the signal region is obtained by applying the fake factors from the determination region on an event-by-event basis to the events in the application region. Via this procedure the complete contribution of all background processes faking a τ_h are obtained in a data-driven manner.

The jet-fake background in the $\tau_h\tau_h$ channel originates almost entirely from QCD multijet events. The determination region is thus defined by inverting the opposite-sign requirement on the di-τ pair to a same-sign requirement. The fake factors are parameterised for the leading τ_h lepton as a function of the p_T of the τ_h. A closure correction for $\vec{p}_T^{\,miss}$ is derived. The jet-flavour composition may differ between the application and determination region. Therefore, another correction to account for the sign inversion of the di-τ_h pair is derived, which is binned in the jet-multiplicity and the distance ΔR between the two jets. The final fake factor for the τ_h channel is obtained by applying the fake factor and the two corrections multiplicatively. This fake factor also accounts for other processes faking a τ lepton such as W + jets production. The events in which the subleading τ_h is a fake jet and the leading τ_h candidate is a genuine τ lepton are modelled via simulation; these events constitute only a small fraction ($\mathcal{O}(2\%)$) of the total fake jet background.

In the $\tau_\mu\tau_h$ channel the W + jets and, to a lesser extend, $t\bar{t}$ processes, contribute to jet misidentification as well as events originating from QCD multijet production. Therefore, separate fake factors are derived for these processes, and their fake factors are subsequently weighted into an overall fake factor to account for their different contributions in the signal region. The overall fake factor accounts for the jet misidentification in all background processes. The procedure for the QCD fake factors is similar to the method as described for the $\tau_h\tau_h$ channel, except that a correction factor is derived for the sign inversion and muon isolation requirement. A determination region sufficiently pure in W + jets is defined by selecting events with muon transverse mass (as defined in Eq. 8) larger than 70 GeV. A correction factor is applied to account for different jet-flavour compositions in the high and low-m_T region, as well as a correction factor for the muon p_T spectrum. For the $t\bar{t}$ process it is difficult to define a sufficiently pure region in data, and thus the jet-fake contribution is estimated from a simulated $t\bar{t}$ sample. For the W + jets and $t\bar{t}$ contributions closure corrections for $\vec{p}_T^{\,miss}$ are derived analogously to the $\tau_h\tau_h$ channel.

After applying the correction factors multiplicatively, we obtain satisfactory closure in the observables that we use to categorise events. This is described in Section 8.

7.3 Corrections

The τ embedding and the fake factor methods describe around 90% of the backgrounds to this analysis. The remaining background is estimated from simulated events. To avoid event double counting, all events with a genuine τ pair or in which a hadronic jet is misidentified as a τ_h are subtracted from all simulated samples. In Table 3 we summarise the different backgrounds and their modelling.

Table 3: The different sources of di-τ backgrounds are depicted on the rows and columns. The entries in the table represent the possible di-τ background contribution from different processes and misidentifications and encapsulate the different experimental techniques that are deployed to estimate the background contributions. Processes involving two prompt leptons, i.e. two electrons, muons, or and electron and a muon, are not considered in this analysis.

	genuine τ_h	jet$\rightarrow\tau_h$	lepton$\rightarrow\tau_h$
genuine τ	τ-Embedding		
jet$\rightarrow\tau$	Fake Factor	Fake Factor	
lepton$\rightarrow\tau$	Simulation	Fake Factor	Simulation
prompt lepton	Simulation	Fake Factor	Simulation

Simulated events are still used to obtain the minor backgrounds involving prompt leptons or

in which a lepton is misidentified as τ_h. In order to model the background processes in data well, various corrections need to be applied to the simulated and embedded event samples.

Muons are corrected for their trigger efficiency, tracking and identification, and isolation requirements. The τ_h are corrected for their trigger efficiency, identification, and energy scale. A tag-and-probe method [70] is used to derive these corrections.

The jet energies are corrected to particle-level energies using data-driven techniques; the corrections range between 10 and 15% in the central and forward region [71], respectively. Residual data-simulation corrections are applied, which are at the percent level. The $\vec{p}_T^{\,miss}$ is adjusted for the effect of jet energy corrections. Corrections to the $\vec{p}_T^{\,miss}$ are applied to reduce the mismodelling of the simulated $Z + jets$, $W + jets$ and Higgs boson samples. The corrections are applied to the simulated events based on the vectorial difference of the measured missing transverse momentum and total transverse momentum of neutrinos originating from the decay of the Z, W, or Higgs boson. Their average effect is the reduction of the p_T^{miss} obtained from simulation by a few GeV. Recoil corrections to p_T^{miss} are measured in $Z \to \mu\mu$ events. The corrections are subsequently applied to the $Z \to \mu\mu$, $W + jets$, and signal simulated event samples. The $l \to \tau_h$ misidentification rates are corrected in simulation, and so are the $l \to \tau_h$ energies, by applying the tag-and-probe method to $Z \to \mu\mu$ events.

The Z mass and p_T spectrum in simulation is corrected to better match the data. A correction is also applied to the top p_T spectrum in the $t\bar{t}$ sample, using a dedicated control region. The procedures of these corrections are detailed in [72].

The impact parameters in the simulated and embedded samples are calibrated using a sample of $Z \to \mu\mu$ events and quantile-mapping techniques. A $Z \to \tau\tau$ sample is used to validate the procedure.

All corrections to the τ lepton decay products must also be applied in the embedded samples. The corrections are known to differ between the embedded samples and the corresponding simulated samples, and therefore dedicated correction factors are derived for embedded events.

Uncertainties for all these corrections are included as nuisance parameters, as explained in Section 11. The systematic uncertainties are outlined in Section 10.

8 Event categorisation

In order to enhance the sensitivity of this analysis, we apply two MVA discriminants to separate signal from background events in the $\tau_\mu\tau_h$ and $\tau_h\tau_h$ channel.

This event categorisation is formulated as a multi-class problem. The discriminant assigns each event to a category depending on the class that received the highest score. Since both the $\tau_\mu\tau_h$ and $\tau_h\tau_h$ channel are dominated by backgrounds containing contributions from genuine and jet-fake processes (which are mainly driven by $Z \to \tau\tau$ and QCD multijet production), the discriminant is trained to categorise events in three classes:

- The events in the Higgs category are used to infer the CP quantum numbers of the boson. This category is trained to distinguish events from the ggH, VBF, and VH samples, which are reweighed by their cross-sections before merging them into one sample.
- The genuine τ category includes all background processes involving two genuine τ leptons.

Table 4: Input variables to the MVA discriminants for the $\tau_\mu\tau_h$ and $\tau_h\tau_h$ channel. For all variables only the visible decay products of the τ leptons are implied, except for the $\tau_\mu\tau_h$ and $\tau_h\tau_h$ mass, for which the SVFIT algorithm is used.

Observable	$\tau_\mu\tau_h$	$\tau_h\tau_h$
p_T of leading τ_h or τ_μ	✓	✓
p_T of (trailing) τ_h for $\tau_\mu\tau_h$ ($\tau_h\tau_h$) channel	✓	×
p_T of visible di-τ	✓	✓
p_T of di-τ_h + p_T^{miss}	×	✓
p_T of $\mu + \tau_h$ + p_T^{miss}	✓	×
Visible di-τ mass	✓	✓
$\tau_\mu\tau_h$ or $\tau_h\tau_h$ mass (using SVFIT)	✓	✓
Leading jet p_T	✓	✓
Trailing jet p_T	✓	×
Jet multiplicity	✓	✓
Dijet invariant mass	✓	✓
Dijet p_T	✓	×
Dijet $\lvert\Delta\eta\rvert$	✓	×
p_T^{miss}	✓	✓

- The jet-fakes category includes all background processes in which minimally one QCD jet is misidentified as τ lepton. For the $\tau_\mu\tau_h$ channel the $l \to \tau_h$ misidentified events and events involving a prompt muon enter in this category as well.

The three categories are mutually exclusive and, by definition, the lower bound for the MVA score is $1/3$. Subsequently, the three training categories are normalised to account for unbalanced data sets. These are normalised using a class weight that scales each training category to a scale such that the classes are overall treated as equally important in the training. For each year a separate training has been performed. The samples are split in two, mutually exclusive, training and prediction samples, such that none of the events are used simultaneously for both training and predictions.

In the $\tau_\mu\tau_h$ channel the event categorisation is performed with a multi-class Neural Network (NN). The architecture of the NN is similar to the one previously used in the study of Higgs decay in τ leptons with machine learning techniques [73]. In the $\tau_h\tau_h$ channel the event categorisation is performed using a BDT algorithm combined with the XGBoost package.

The input variables used in the categorisation of the $\tau_\mu\tau_h$ and $\tau_h\tau_h$ are displayed in Table 4. This is a subset of the variables employed in [73], in which these were reviewed to have good discriminating power between the different processes. Furthermore, it was inferred in [73] via a Taylor expansion that the di-τ mass (using SVFIT) and the visible di-τ mass contribute most to the power of the MVA to distinguish between signal and background events. The training is performed inclusively for all the τ decay modes. After the categorisation a cutoff of $S_{IP} > 1.5\sigma_{S_{IP}}$ is applied to the impact parameter significances of the μ as well as the pion of the τ decay to a single pion.

In Fig. 3 the postfit NN scores of the genuine τ (left), and jet-fakes (right) categories for the $\tau_\mu\tau_h$ channel are displayed. The best-fit signal contributions are overlaid. The genuine τ background contributions are indicated with $\mu \to \tau_h$ Embed. The jet-fake contributions are indicated with $j \to \tau_h$. The remaining contributions from the backgrounds that are considered in

this analysis are collective indicated by the Others label. The BDT scores for the $\tau_h\tau_h$ channel are analogously displayed in Fig. 4.

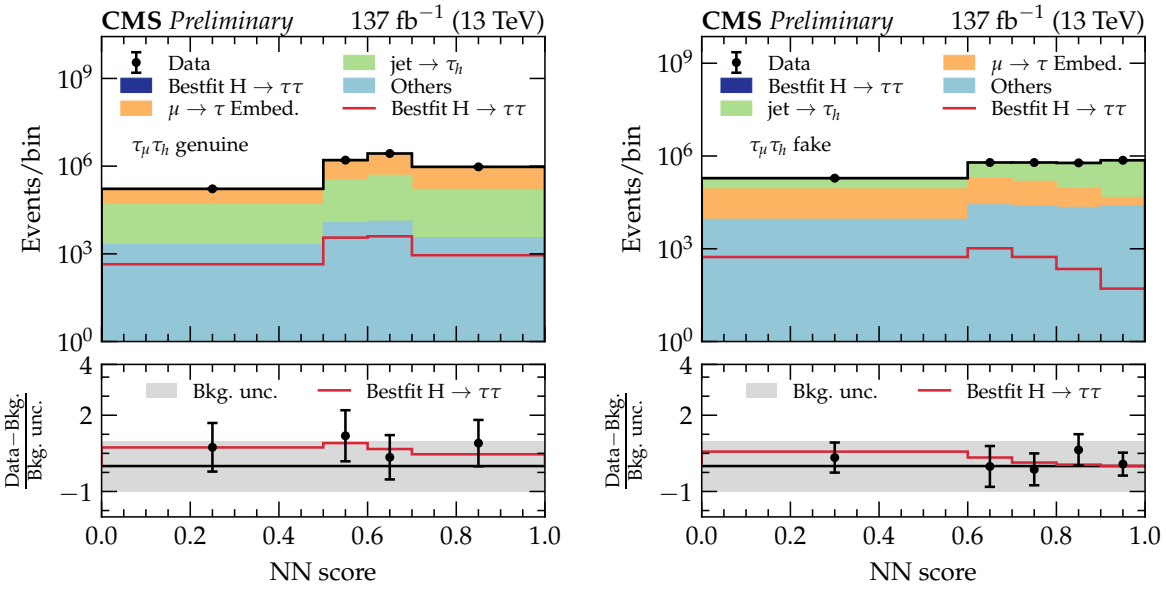

Figure 3: The postfit genuine τ (left), and jet-fake (right) NN scores for the $\tau_\mu\tau_h$ channel. The distributions are inclusive in decay mode. The best-fit signal distributions are overlaid. In the bottom plot the data minus the background template divided by the uncertainty in the background template is displayed, as well as the signal samples divided by the uncertainty in the background template. The uncertainty band consists of the sum of the postfit uncertainties in the background templates.

9 The ϕ_{CP} distributions in windows of multivariate discriminant score

The MVA score distributions described in Section 8 allow for a partial separation of signal from background events. The ϕ_{CP} distributions of the events in the signal category are then analysed in windows of increasing MVA score. These windows correspond to progressively higher signal/background ratios and are effectively unrolled two-dimensional histograms of MVA score on one axis and ϕ_{CP} on the other.

The statistical fluctuations in the background templates, i.e. the estimates of the background contributions in the signal and background categories, are sizeable. It is known [30] that backgrounds involving two genuine τ leptons are flat in ϕ_{CP} at particle level. Experimental smearing effects do not modulate this flat shape for methods in which we apply the neutral pion method for at least one τ lepton. Therefore, for this background process and decay modes we flatten the background templates by merging the bins. The ϕ_{CP} distribution is not flat for the jet-fake background for all decay modes due to the kinematic properties of the event, but the distributions are still symmetric in $\phi_{CP} = 180°$, and so the background is symmetrised. For other background templates, for example the $\mu \to \tau_h$ contribution, the distributions are found to be flat within the statistical uncertainties, and therefore these backgrounds are also flattened.

The backgrounds are not expected to be flat in decay modes in which the impact parameter method is applied twice, but rather symmetric in $\phi_{CP} = 180°$. This can be understood from

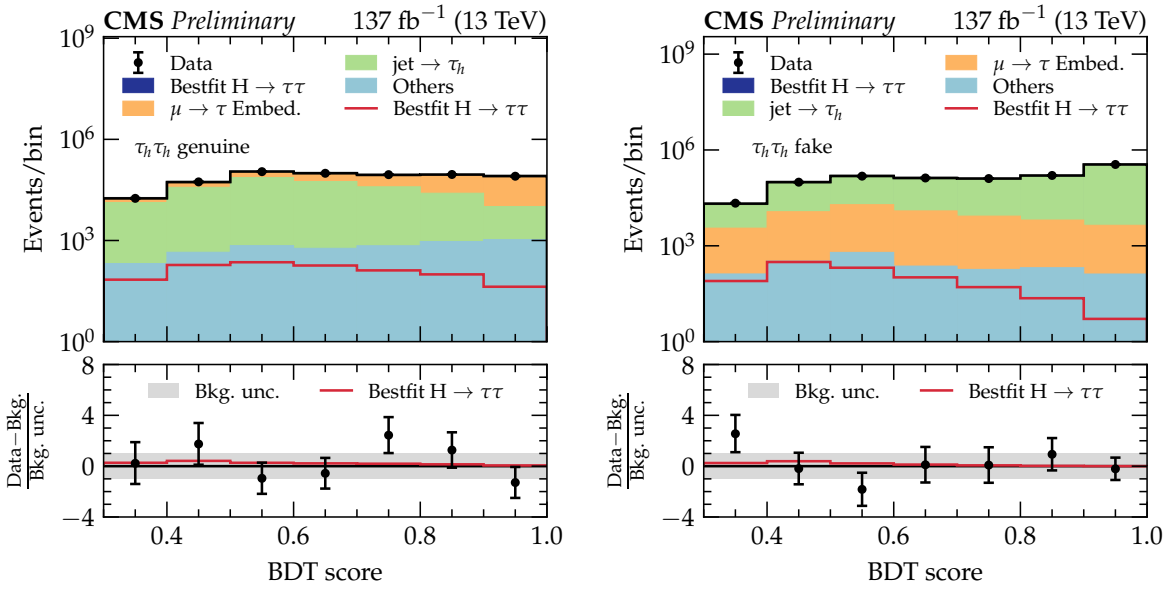

Figure 4: The postfit genuine τ (left), and jet-fake (right) BDT scores for the $\tau_h\tau_h$ channel. The distributions are inclusive in decay mode. The best-fit signal distributions are overlaid. In the bottom plot the data minus the background template divided by the uncertainty in the background template is displayed, as well as the signal samples divided by the uncertainty in the background template. The uncertainty band consists of the sum of the postfit uncertainties in the background templates.

the fact that smearing effects in the primary vertex are correlated for the decay planes. The smearing of the PV results in a depletion in the region $\phi_{CP} = 180^\circ$ [74]. Therefore, for these channels a bin symmetrisation is applied to all background templates.

For certain decay modes the statistical fluctuations in the signal templates are also sizeable. Therefore, the templates of the (speudo) scalar are symmetrised in $\phi_{CP} = 180^\circ$ as well. The maximally mixed signal template, which is not displayed in the plots but used in the fitting procedure described in Section 11, is symmetrised as well. This is accomplished by symmetrising in $\phi_{CP} = 180^\circ$ with a signal template with $\phi_{\tau\tau} = -45^\circ$.

In Fig. 5 and Fig. 6 we display the postfit unrolled distributions for the data and background template distribution, after the bin smearing and symmetrisation for the Higgs category, with the best-fit and pseudoscalar signal templates overlaid. The four most sensitive decay modes of the analysis are displayed, which are the $\mu\rho$ and $\mu\pi$ mode, displayed in Fig. 5 top and bottom, respectively, and the $\rho\rho$ and $\pi\rho$ mode, displayed in Fig. 6 top and bottom, respectively. The distributions clearly show the crucial role of the MVA discriminant in optimising the signal over background ratio, as well as the CP-sensitivity of the measurement, which can be inferred from the visibly different phases of the best-fit signal and CP-odd signal distributions. The 180° phase shift between the $\tau_h\tau_h$ and $\tau_\mu\tau_h$ channel is also visible in the figures.

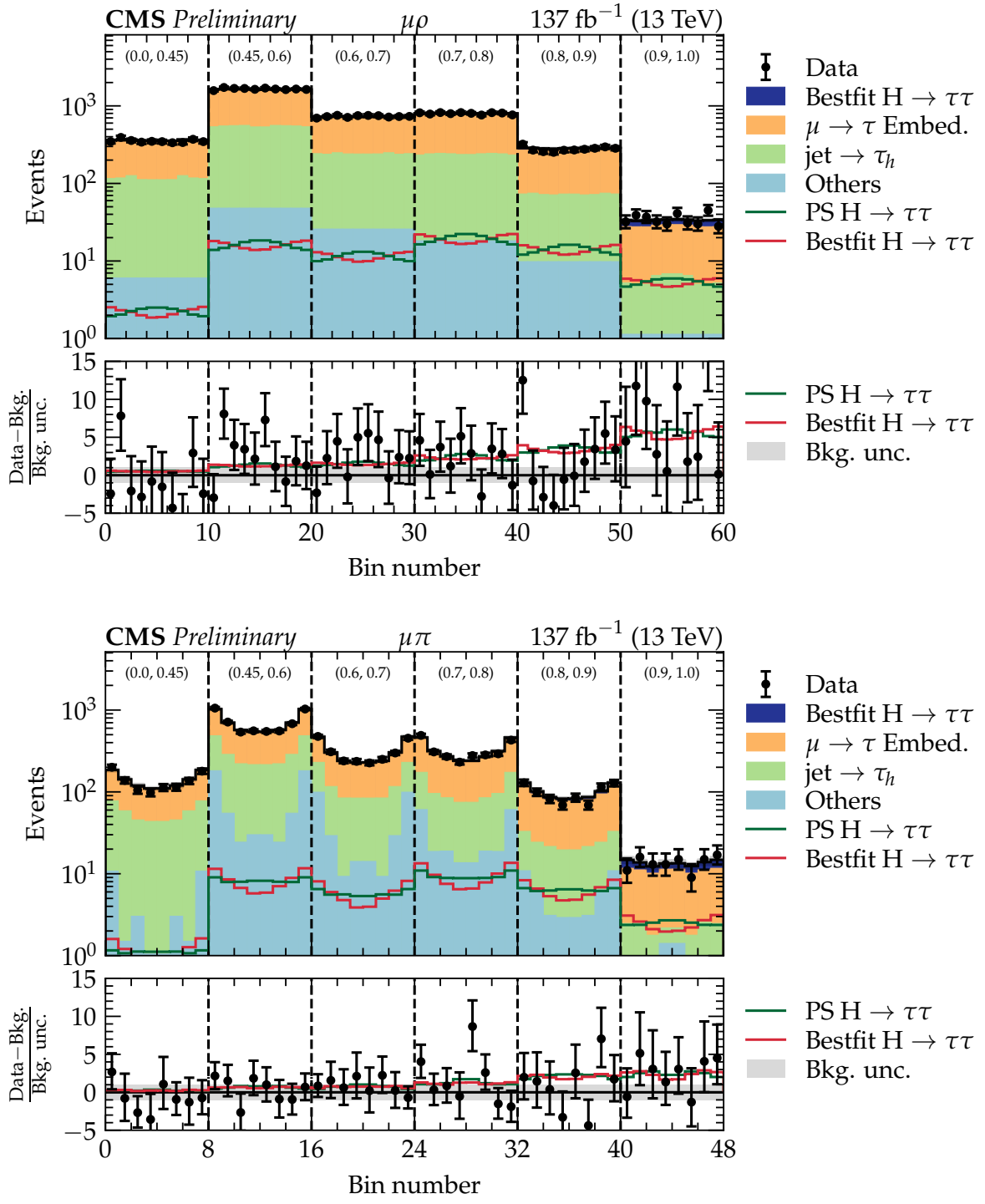

Figure 5: Distributions of ϕ_{CP} in the $\mu\rho$ (top) and $\mu\pi$ (bottom) channel in windows of increasing neural net score. The best-fit and pseudoscalar (PS) signal distributions are overlaid. The x axis represents the cyclic bins in ϕ_{CP} in the range of $(0, 360^\circ)$. In the bottom plot the data minus the background template divided by the uncertainty in the background template is displayed, as well as the signal samples divided by the uncertainty in the background template. The uncertainty band consists of the sum of the postfit uncertainties in the background templates.

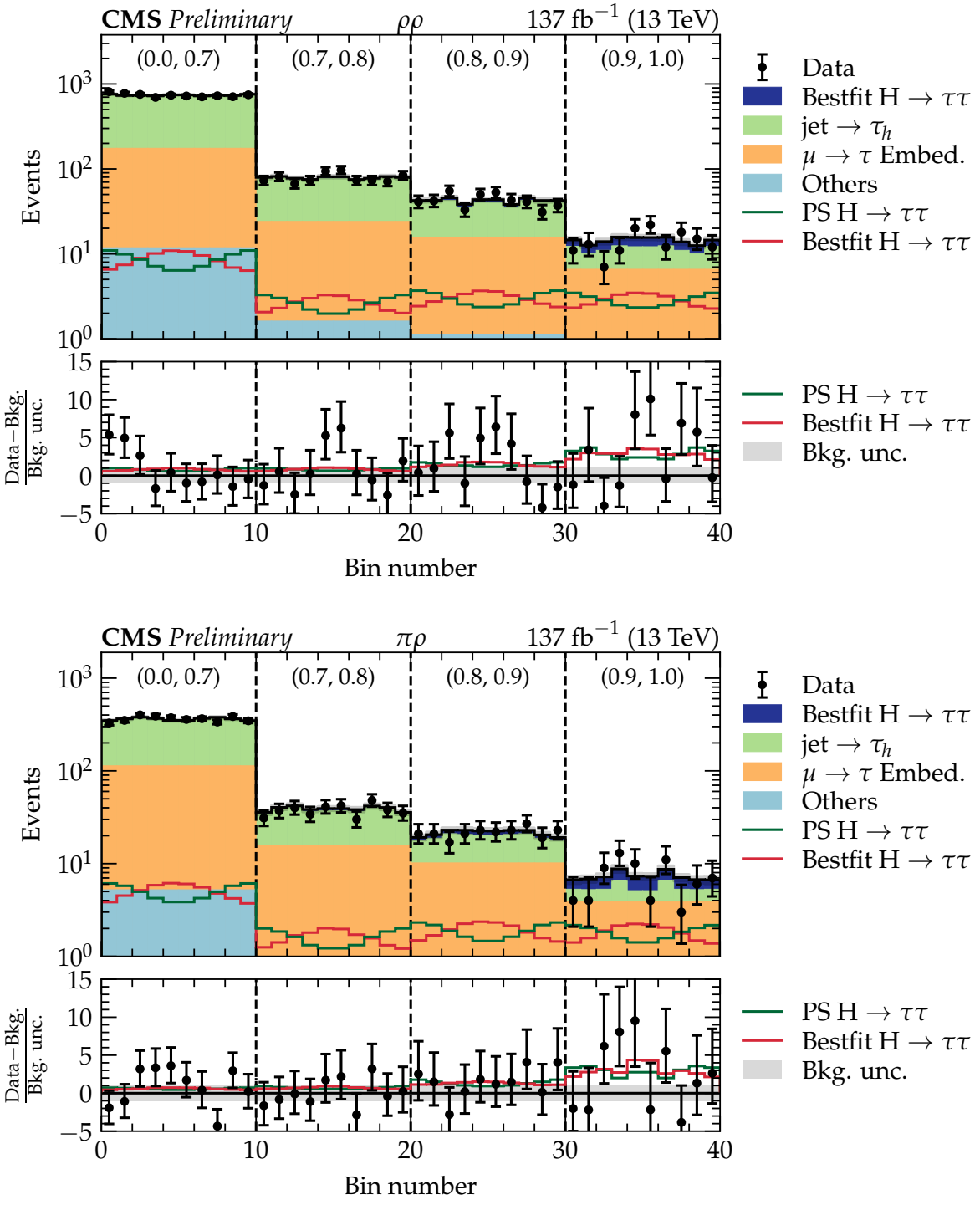

Figure 6: Distributions of ϕ_{CP} in the $\rho\rho$ (top) and $\pi\rho$ (bottom) channel in windows of increasing BDT score. The best-fit and pseudoscalar (PS) signal distributions are overlaid. The x axis represents the cyclic bins in ϕ_{CP} in the range of $(0, 360°)$. In the bottom plot the data minus the background template divided by the uncertainty in the background template is displayed, as well as the signal samples divided by the uncertainty in the background template. The uncertainty band consists of the sum of the postfit uncertainties in the background templates.

10 Systematic uncertainties

The uncertainties considered in this analysis can be categorised into normalisation, shape, and statistical uncertainties. Generally, uncertainties that are split by decay mode are treated as uncorrelated between the decay modes. The uncertainties are summarised in Table 5, in which we also state their correlations between the three different years of data taking considered in this analysis.

10.1 Normalisation uncertainties

The luminosity uncertainty amounts to 2.5, 2.3, and 2.5% for 2016, 2017, and 2018 respectively [75–77], and is applied to all simulated samples discussed in Section 4.

The uncertainty on the muon reconstruction efficiency including the tracking, identification, and isolation requirements is 1%, while the uncertainty in the trigger efficiency is 2% per muon leg. Consequently, a normalisation uncertainty of 4% is applied to the embedded event samples, originating from the uncertainty on the measurement of the muon identification and trigger efficiencies used to scale the embedded samples.

For the $\tau_\mu\tau_h$ channel, which contains a veto on events containing b jets, an uncertainty in the propagation of b-quark tagging scale factors of 1–9% is applied on the $t\bar{t}$ and diboson processes event yields (the uncertainties on the event yields for other simulated processes are found to be negligible).

The FEWZ 3.1 program [78] was used to calculate the $W+$jets and $Z+$jets cross sections. For the Z+jets an additional integration uncertainty was included. The TOP++V2.0 program [79] was used to calculate the $t\bar{t}$ cross section and its uncertainty. Uncertainties in the factorisation and renormalisation scale, the PDF, the running coupling α_S, and the top quark mass were propagated and added in quadrature. The extracted uncertainties for the simulated $Z+$jets, $W+$jets, and $t\bar{t}$ processes amount to 2, 4, and 4%, respectively. For the diboson and single top quark production processes a combined systematic uncertainty on the background yield is estimated to be 5% using CMS measurements [80, 81].

The uncertainty in the $\mu \to \tau_h$ misidentification is split into four independent uncertainties depending on the MVA decay mode of the $\mu \to \tau_h$ candidate. The sizes of the uncertainties are 20% for π and ρ, 30% for a_1^{1pr}, and 40% for a_1^{3pr} and $\tau_h \to \pi^\pm\pi^\mp\pi^\pm\pi^0$, respectively. The uncertainties in the signal ggH, VBF and VH production cross sections, as well as the uncertainty in the $H \to \tau\tau$ branching fraction, are applied as recommended in [82].

An uncertainty of 5 (1)% to the $e \to \tau_h$ fake rate is applied for 2016 (2017, 2018) in the $\tau_h\tau_h$ channel. In 2016 and 2017 prefiring in the ECAL calorimeter system occurred. The magnitude of the effect of this uncertainty ranges between 0-4% depending on the process, category, and channel.

A normalisation uncertainty in the correction factor for the QCD same-sign opposite-sign regions is determined as the magnitude of the unbinned correction factor.

10.2 Shape uncertainties

The τ_h reconstruction/identification efficiency is typically of the order of 3%, and split into several uncertainties in each p_T and MVA decay mode bin. The uncertainty in these corrections originates from uncertainties in the fits to the scale factors for these corrections. The uncertainty is statistically dominated and of the order of 3%. The uncertainty in the τ_h trigger depends on the p_T and decay mode, and originates from the statistical uncertainty in parameterising

the turn-on curve of the triggers. The τ_h energy scale uncertainty is 0.8–1.1 (0.2–0.5)% for simulated (embedded) events, and decay-mode dependent. The uncertainty in the μ energy scale varies as function of its pseudorapidity and ranges between 0.4-2.7%. The $e \to \tau_h$ energy scale uncertainty ranges 0.5–6.5%, while the $\mu \to \tau_h$ energy scale uncertainty is 1%. For the $\tau_\mu \tau_h$ channel, a rate uncertainty of 20–40% for the $\mu \to \tau_h$ process is applied. Uncertainties in the jet energy scale originate from different sources with limited correlations. The uncertainties depend on the jet kinematics and are typically larger in the forward regions.

Uncertainties in the jet energy resolution are also incorporated; these uncertainties are typically smaller than the jet energy scale uncertainties. Uncertainties in the missing transverse energy are propagated for simulated samples in which recoil corrections are applied. For the other processes (diboson, single top, and $t\bar{t}$), uncertainties in the unclustered energy scale are propagated, and the magnitude of the corrections are event-dependent.

The embedded samples contain small fractions of $t\bar{t}$ and diboson events. A shape uncertainty is therefore applied by adding and subtracting 10% of the $t\bar{t}$ and diboson contributions of simulated samples. The top and Drell-Yan p_T spectra are reweighed. For the top samples the correction is applied twice as uncertainty, while for the Drell-Yan the reweighing is varied by 10%.

The fake factors are parameterised with continuous functions, and the statistical uncertainties in the fitted parameters are treated as nuisance parameters for the QCD and W + jets corrections. The uncertainties are parameterised in a manner that allows for asymmetric variation above and below the p_T-value where the uncertainty is minimal, the procedure is similar to the method described in detail in [7]. The non-closure correction in E_T^{miss} is applied twice for the upwards and not for the downwards variation as uncertainty for all fake factors. The shape uncertainty in the QCD same-sign opposite-sign region correction is determined as the difference between a correction binned in the distance ΔR between the two τ leptons and the jet-multiplicity, and the unbinned correction. In addition, for the $\tau_\mu \tau_h$ channel a systematic uncertainty due to the muon p_T non-closure correction is defined by applying the correction twice for the upward and not for the downward variation. For the W + jets fake factors furthermore the uncertainty in the high-m_T versus low-m_T region is defined by applying the correction twice for the upward and not for the downward variation. For the $t\bar{t}$ fake factor a systematic uncertainty is applied to account for potential differences between data and simulation. To this purpose, the difference between fake factors derived via data and simulated W + jets samples is applied as uncertainty.

For uncertainties that are common to simulated and embedded samples we treat the lepton and τ_h identification uncertainties and the lepton and τ_h energy scale uncertainties as being 50% correlated. All other common uncertainties are treated as being uncorrelated.

For the μ and π decays an uncertainty on the correction of S_{IP} is applied by varying the size of the correction by $\pm 25\%$.

Limitations in the event statistic of the signal and background templates are accounted for using the "Barlow-Beeston" method, which assigns a single nuisance parameter per bin per process [83, 84]. For background templates which have been flattened as described in Section 8 the bin-by-bin uncertainties are fully correlated such that there is only one independent nuisance parameter for all ϕ_{CP} bins of the flattened backgrounds. For background templates that are symmetric in $\phi_{CP} = 180^\circ$ one nuisance parameter per pair of symmetrised bins is utilised. It should be noted that for flattened backgrounds still multiple nuisance parameters are needed per process since multiple windows of increasing NN/BDT score are used.

Table 5: Sources of systematic uncertainties. The third column indicates if the source of uncertainty was treated as being correlated between the years in the fit described in Section 11. The fourth column indicates the probability density for the uncertainty applied in the fit

Uncertainty	Magnitude	Correlation	Incorp. fit
τ_h ID	p_T/decay-mode dependent (2–3%)	no	Gaussian
Muon reconstruction	1%.	yes	log-normal
$e \to \tau_h$ ID	5(1)% 2016(2017,2018)	no	Gaussian
$\mu \to \tau_h$ ID	20–40%	no	Gaussian
μ ID	1%	yes	Gaussian
b-jet veto	1–9%	no	log-normal
Luminosity	2.5%	partial	log-normal
Trigger	2% for μ, p_T-dep. for τ_h	no	Gaussian
Embedded yield	4%	no	log-normal
$t\bar{t}$ cross section	4.2%	yes	log-normal
Diboson cross section	5%	yes	log-normal
Single top cross section	5%	yes	log-normal
W + jets cross section	4%	yes	log-normal
Drell-Yan cross section	2%	yes	log-normal
Signal cross sections	[82]	yes	log-normal
top p_T reweighing	10%	yes	Gaussian
Z p_T reweighing	10%	partial	Gaussian
Prefiring (2016, 2017)	Event-dependent (0–4%)	yes	log-normal
τ_h energy scale	1% (sim), 1.5% (emb.)	no	Gaussian
$e \to \tau_h$ energy scale	0.5–6.5%	no	log-normal
$\mu \to \tau_h$ energy scale	1%	no	log-normal
Muon energy scale	0.4–2.7%	yes	Gaussian
Jet energy scale	Event-dependent	partial	Gaussian
Jet energy resolution	Event-dependent	no	Gaussian
p_T^{miss} unclustered scale	Event-dependent	no	Gaussian
p_T^{miss} recoil corrections	Event-dependent	no	Gaussian
Jet$\to \tau_h$ mis-ID	described in text	partial	Gaussian
$t\bar{t}$/diboson in embedded	10%	yes	Gaussian
S_{IP} in μ and π decays	25%	no	Gaussian

11 Results

In order to extract the CP-mixing angle $\phi_{\tau\tau}$, a simultaneous fit to the data is performed using the likelihood function, $L(\vec{\mu}, \mu^{\tau\tau}, \phi_{\tau\tau}, \vec{\theta})$ that depends on $\vec{\mu} = (\mu_{\mathrm{ggH}}, \mu_{\mathrm{qqH}})$, which is the Higgs boson production signal strength modifier with respect to the SM value, the branching fraction modifier with respect to the SM value $\mu^{\tau\tau}$ of $\mathrm{H} \to \tau\tau$ decay, the CP-mixing angle $\phi_{\tau\tau}$, and the nuisance parameters $\vec{\theta}$ that account for the systematic uncertainties. In this equation, $\mu_{\mathrm{qqH}} = (\mu_{\mathrm{VBF}}, \mu_{\mathrm{WH}}, \mu_{\mathrm{ZH}})$, i.e. all Higgs vector boson couplings are scaled by a single parameter in the fit. The likelihood function is defined as a product of conditional probabilities P over binned distributions of the discriminating observables in each event category j,

$$L(\vec{\mu}, \mu^{\tau\tau}, \phi_{\tau\tau}, \vec{\theta}) = \prod_{j}^{N_{\mathrm{categories}}} \prod_{i}^{N_{\mathrm{bin}}} P(n_{i,j} \mid \mathcal{L} \cdot \vec{\mu} \cdot \mu^{\tau\tau} \cdot \vec{A}_{i,j}(\vec{\theta}, \phi_{\tau\tau}) + B_{i,j}(\vec{\theta})) \times \prod_{m}^{N_{\mathrm{nuisance}}} C_m(\vec{\theta}), \tag{9}$$

with Poisson distributions P corresponding to the observation of $n_{i,j}$ events in each bin i of the discriminating observable given the expectation for the background $B_{i,j}(\vec{\theta})$, and for the signal $S_{i,j}(\vec{\theta}) = \mathcal{L} \cdot \vec{\mu} \cdot \mu^{\tau\tau} \cdot \vec{A}_{i,j}(\vec{\theta}, \phi_{\tau\tau})$, where $\mathcal{L}$ is the integrated luminosity and $\vec{A}_{i,j}(\vec{\theta}, \phi_{\tau\tau})$ is the signal acceptance in each production bin. Constraints on the nuisance parameters corresponding to the systematic uncertainties described in Section 10 are represented by the functions $C_m(\vec{\theta})$. A more detailed discussion on the ingredients of the statistical inference may be found in [84, 85].

The systematic uncertainties affecting the normalisation of the signal and background templates are incorporated in the fit via nuisance parameters with a log-normal prior probability density function. The shape-altering systematic uncertainties are represented by nuisance parameters whose variations cause continuous morphing of the signal or background template shape, and are assigned a Gaussian prior probability density function. The bin-by-bin statistical uncertainties in the background samples are also assigned a Gaussian prior probability density function.

Using the negative log-likelihood, which is defined as

$$-2\Delta \ln L = -2 \cdot \left(\ln(L\phi_{\tau\tau}) - \ln(L\phi_{\tau\tau}^{\text{best fit}}) \right), \tag{10}$$

we may find the 68, 95, and 99.7% confidence intervals when $-2\Delta \ln L = 1.00$, 3.84, and 8.81, respectively. A detailed discussion may be found in Section 3.2 of Ref. [86].

The inputs to the likelihood fits differ for the signal and background categories. For the signal category, the ϕ_{CP} distribution for each τ decay mode combination is used, in bins of NN or BDT score (as examples these were displayed for the most sensitive decay modes in Fig. 5 and 6, respectively). For the background categories the NN and BDT score distributions are utilised inclusively for the $\tau_\mu\tau_{\mathrm{h}}$ and $\tau_{\mathrm{h}}\tau_{\mathrm{h}}$ channel, respectively. This allows the background contributions and systematic uncertainties to be further constrained, and helps to improve the fit convergence.

11.1 $\phi_{\tau\tau}$ mixing angle results

We present the expected negative log-likelihood scan for the combination of the $\tau_\mu\tau_{\mathrm{h}}$ and $\tau_{\mathrm{h}}\tau_{\mathrm{h}}$ channels in Fig. 7. The two rate parameters that scale the ggH and qqH production signal

strength were left to float freely in the fit. As we cannot disentangle $\mu^{\tau\tau}$ from the production signal strength modifiers in the fit, $\mu^{\tau\tau}$ is fixed to unity.

The fit allows us to distinguish between scalar and pseudoscalar H$\tau\tau$ coupling hypotheses at an observed (expected) sensitivity of 3.2 (2.3) standard deviations. The observed (expected) value of $\phi_{\tau\tau}$ is found to be $4 \pm 17^\circ$ ($0 \pm 23^\circ$) at the 68% CL, and $\pm 36^\circ$ ($\pm 55^\circ$) at the 95% CL. Furthermore, we obtain an observed $\pm 66^\circ$ at the 99.7% CL. The uncertainty can be decomposed into the following components: statistical, bin-by-bin fluctuations in the background samples, experimental systematical uncertainties, and theoretical uncertainties. In this decomposition we obtain $\phi_{\tau\tau} = (4 \pm 17\,(\text{stat}) \pm 2(\text{bin-by-bin}) \pm 1\,(\text{syst}) \pm 1(\text{theory}))^\circ$.

This result is compatible with the standard model predictions within the experimental uncertainties.

The expected sensitivity of the $\tau_h\tau_h$ channel is 1.8σ, while the $\tau_\mu\tau_h$ channel contributes with 1.5σ. The $\mu\rho$ mode yields the most sensitive expected contribution of 1.2σ, followed by the $\rho\rho$ and $\rho\pi$ modes that contribute 1.1 and 1.0σ, respectively. All other modes have sensitivities below 1σ.

The statistical uncertainties in the background templates are one of the driving sources of systematic uncertainty in this analysis. As the dominant contributions to the backgrounds are determined themselves in a data-driven manner, the amount of data itself is the limiting factor in this uncertainty. This source of uncertainty is followed by the hadronic trigger efficiency, theory uncertainties, the τ energy scale, and the fake factor method.

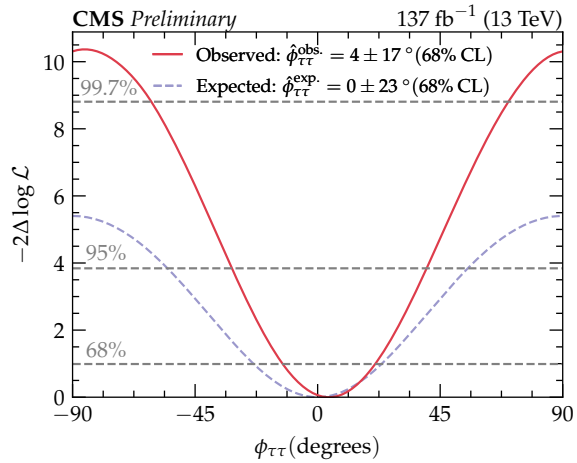

Figure 7: Negative log-likelihood scan for the combination of the $\tau_\mu\tau_h$ and $\tau_h\tau_h$ channel. The observed (expected) sensitivity to distinguish between the scalar and pseudo-scalar hypotheses, defined at $\phi_{\tau\tau} = 0$ and $\pm 90^\circ$, respectively, is 3.2 (2.3) standard deviations. The observed (expected) value for $\phi_{\tau\tau}$ is $4 \pm 17^\circ$ ($0 \pm 23^\circ$) at the 68% CL, at the 95% CL the value is $\pm 36^\circ$ ($\pm 55^\circ$), and at the 99.7% CL we obtain an observed $\pm 66^\circ$.

As a cross check on the results, we extract the overall value of the Higgs production signal strength modifier μ with respect to the predictions of the standard model. A dedicated fit was performed with a single common rate parameter μ to simultaneously scale two rate parameters μ_{ggH} and μ_{qqH}. In the fit $\mu^{\tau\tau}$ was kept fixed at unity. The extracted observed (expected) value is 0.82 ± 0.15 (1.0 ± 0.17); the value is invariant whether we fix $\phi_{\tau\tau}$ to its SM value or let it float in the fit. The value is compatible with what was obtained by a dedicated coupling analysis [73].

In Fig. 8 we display a scan of the branching fraction modifier with respect to the SM value $\mu^{\tau\tau}$

versus $\phi_{\tau\tau}$. We observe that there is no strong correlation between these. In this fit the signal strength modifiers $\vec{\mu}$ were fixed to their SM expectation values.

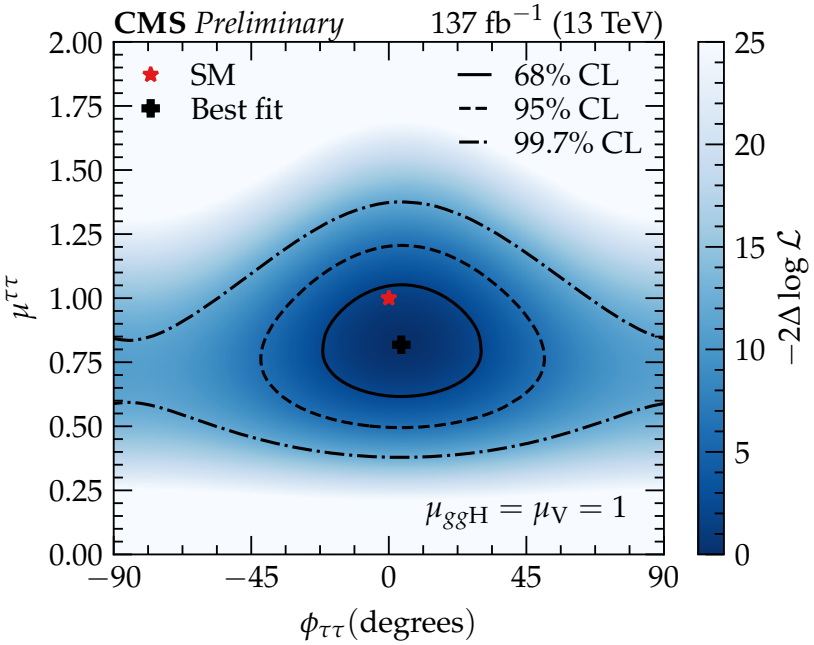

Figure 8: Two-dimensional scan of the branching fraction modifier with respect to the SM value $\mu^{\tau\tau}$ versus $\phi_{\tau\tau}$. All other Higgs couplings are fixed to the SM expectation values.

In order to make a two-dimensional scan of κ_τ and $\tilde{\kappa}_\tau$, as defined in Eq. 2, we parameterise the likelihood from Eq. 9 in terms of κ_τ and $\tilde{\kappa}_\tau$. All other Higgs couplings are fixed to the SM expectation values.

In the case of a two-dimensional negative log-likelihood the 68, 95, and 99.7% confidence intervals are found when $-2\Delta \ln L_{2D} = 2.30$, 5.99, and 11.62 [86], which is defined analogously as in Eq. 10, where the likelihood is now a function of both κ_τ and $\tilde{\kappa}_\tau$. The observed result of the scan is shown in Fig. 9. It can be observed that the best-fit results are located in the upper-right and lower-left quadrant. This may be explained from the fact that the fit is only sensitive to the relative sign between κ_τ and $\tilde{\kappa}_\tau$.

In Fig. 10 we display the data of the three most sensitive channels together with CP-even and odd predictions. The data have been reweighed for an enhanced visual interpretation. This distribution shows that the enhanced significance of the data with respect to the expected significance is because the difference between the data and the CP-odd prediction is larger than the difference between the CP-even and odd prediction due to statistical fluctuations.

In the next-to-minimal supersymmetric model $\phi_{\tau\tau}$ is not allowed to exceed 27° [29]; our result thus excludes a part of the phase space of this model at the 68% confidence level. Furthermore, the observed (expected) uncertainty in the mixing angle, which is $\pm 17°$ $(\pm 23)°$ at the 68% CL, is smaller than the expected uncertainty of $(\pm 27)°$ predicted in [30] for a slightly larger data set of 150 fb^{-1}. Various explanations can be offered for the minor difference in sensitivity as in [30] different kinematical cuts were used, and the experimental smearing effects had to be estimated.

For comparison, pure CP-odd Htt couplings were excluded with 3.2 and 3.9 standard deviations by the CMS [26] and ATLAS [27] Collaborations for comparably-sized data sets in the

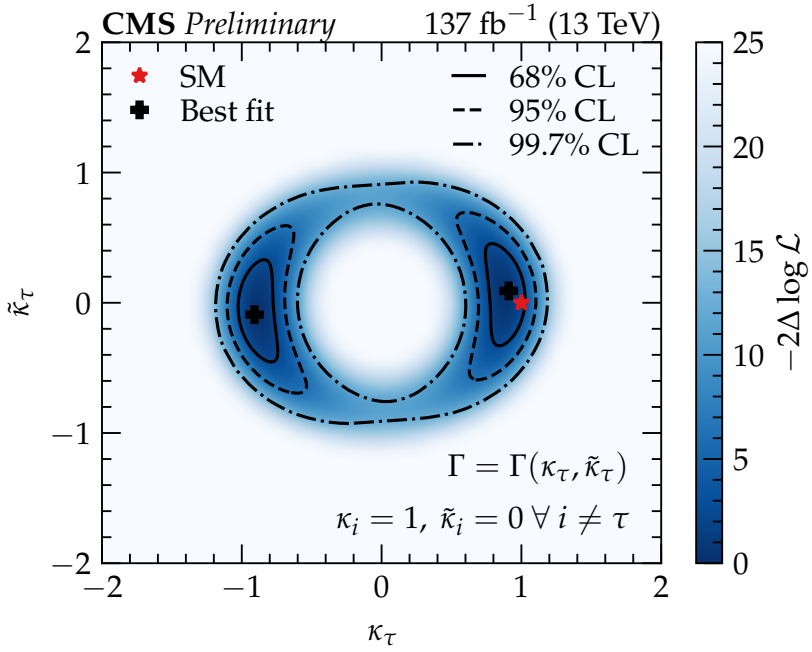

Figure 9: Two-dimensional scan of the (reduced) CP-even (κ) and CP-odd ($\tilde{\kappa}$) τ Yukawa couplings.

most sensitive Htt decay mode. Uncertainties in the mixing angles at the 95% CL level of $\pm 55^\circ$ (CMS) and $\pm 43^\circ$ (ATLAS) were obtained.

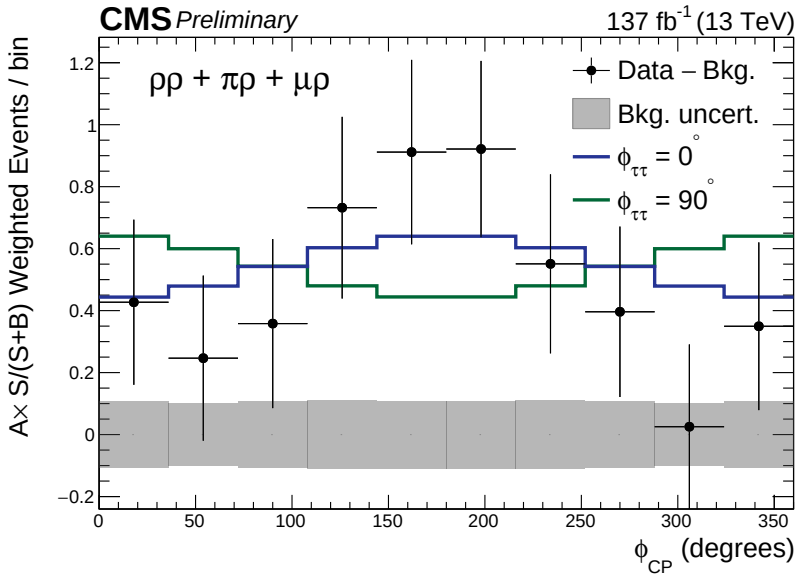

Figure 10: The ϕ_{CP} distribution for the three most sensitive channels combined. Events were collected from all years and NN/BDT bins in the three signal categories. The background is subtracted from the data. The events are reweighed via $A\,S/(S+B)$, in which S and B are the signal and background rates, respectively, and A is a measure for the average asymmetry between the scalar and pseudoscalar distributions. The definition of the value of A per bin is $|\mathrm{CP}^{\mathrm{even}} - \mathrm{CP}^{\mathrm{odd}}|/(\mathrm{CP}^{\mathrm{even}} + \mathrm{CP}^{\mathrm{odd}})$, and A is normalised to the total number of bins. In this equation $\mathrm{CP}^{\mathrm{even}}$ and $\mathrm{CP}^{\mathrm{odd}}$ are the scalar and pseudoscalar contributions per bin. The scalar distribution is depicted in blue, while the pseudoscalar is displayed in green. In the predictions, the rate parameters are taken from their best-fit values. The grey uncertainty band indicates the uncertainty on the subtracted background component. In combining the channels, a phase-shift of 180° was applied to the channel involving a muon since this channel has a phase difference of 180° with respect to the two hadronic channels due to a sign-flip in the muon spectral function.

12 Summary

The first measurement of the effective mixing angle $\phi_{\tau\tau}$ between a scalar and pseudoscalar $H\tau\tau$ coupling has been presented for a data set of pp collisions at $\sqrt{s} = 13\,\text{TeV}$ of 137 fb^{-1}. The data were collected with the CMS experiment at the LHC in the period 2016–2018. The fully hadronic channel was included as well as the $\tau_\mu\tau_h$ channel, in which one τ lepton decayed via a muon and the other to hadrons. Machine learning techniques were applied to separate the signal from background events and distinguish between the hadronic τ decay modes. Dedicated strategies were adopted to reconstruct the angle ϕ_{CP} between the τ decay planes for the various τ decay modes, and the reconstruction of the primary vertex was optimised for the measurement. The hypothesis for a pure CP-odd pseudoscalar boson is rejected with 3.2 (2.3) observed (expected) standard deviations. The observed mixing angle is found to be $4 \pm 17^\circ$, while the expected value is determined as $0 \pm 23^\circ$ at the 68% confidence level. At the 95% confidence level the observed and expected uncertainties are found to be $\pm 36^\circ$ and $\pm 55^\circ$, respectively, and the observed sensitivity at the 99.7% CL is $\pm 66^\circ$. The $\mu\rho$ channel is estimated to be the most sensitive mode, followed by the $\rho\rho$ and $\pi\rho$ channels. The driving uncertainties in the measurement presented are of statistical nature, implying that the precision of the measurement will increase with the accumulation of more collision data. The measurement is consistent with the standard model expectation, and reduces the allowed parameter space for extensions of the standard model.

References

[1] F. Englert and R. Brout, "Broken symmetry and the mass of gauge vector mesons", *Phys. Rev. Lett.* **13** (1964) 321, doi:10.1103/PhysRevLett.13.321.

[2] P. W. Higgs, "Broken symmetries and the masses of gauge bosons", *Phys. Rev. Lett.* **13** (1964) 508, doi:10.1103/PhysRevLett.13.508.

[3] G. S. Guralnik, C. R. Hagen, and T. W. B. Kibble, "Global conservation laws and massless particles", *Phys. Rev. Lett.* **13** (1964) 585, doi:10.1103/PhysRevLett.13.585.

[4] ATLAS Collaboration, "Observation of a new particle in the search for the Standard Model Higgs boson with the ATLAS detector at the LHC", *Physics Letters B* **716** (2012), no. 1, 1, doi:10.1016/j.physletb.2012.08.020, arXiv:1207.7214.

[5] CMS Collaboration, "Observation of a new boson at a mass of 125 GeV with the CMS experiment at the LHC", *Physics Letters B* **716** (2012), no. 1, 30, doi:10.1016/j.physletb.2012.08.021, arXiv:1207.7235.

[6] ATLAS, CMS Collaboration, "Measurements of the Higgs boson production and decay rates and constraints on its couplings from a combined ATLAS and CMS analysis of the LHC pp collision data at $\sqrt{s} = 7$ and 8 TeV", *JHEP* **08** (2016) 045, doi:10.1007/JHEP08(2016)045, arXiv:1606.02266.

[7] CMS Collaboration, "Observation of the Higgs boson decay to a pair of τ leptons with the CMS detector", *Physics Letters B* **779** (2018) 283, doi:10.1016/j.physletb.2018.02.004, arXiv:1708.00373.

[8] ATLAS Collaboration, "Cross-section measurements of the Higgs boson decaying into a pair of τ-leptons in proton-proton collisions at a centre-of-mass energy of 13 TeV with the

ATLAS detector", *Physical Review D* **99** (2019), no. 7, doi:10.1103/physrevd.99.072001, arXiv:1811.08856.

[9] CMS Collaboration, "On the mass and spin-parity of the Higgs boson candidate via its decays to Z boson pairs", *Phys. Rev. Lett.* **110** (2013) 081803, doi:10.1103/PhysRevLett.110.081803, arXiv:1212.6639.

[10] CMS Collaboration, "Measurement of the properties of a Higgs boson in the four-lepton final state", *Phys. Rev. D* **89** (2014) 092007, doi:10.1103/PhysRevD.89.092007, arXiv:1312.5353.

[11] CMS Collaboration, "Constraints on the spin-parity and anomalous HVV couplings of the Higgs boson in proton collisions at 7 and 8 TeV", *Phys. Rev. D* **92** (2015) 012004, doi:10.1103/PhysRevD.92.012004, arXiv:1411.3441.

[12] CMS Collaboration, "Limits on the Higgs boson lifetime and width from its decay to four charged leptons", *Phys. Rev. D* **92** (2015) 072010, doi:10.1103/PhysRevD.92.072010, arXiv:1507.06656.

[13] CMS Collaboration, "Combined search for anomalous pseudoscalar HVV couplings in VH(H $\to b\bar{b}$) production and H $\to$ VV decay", *Phys. Lett. B* **759** (2016) 672, doi:10.1016/j.physletb.2016.06.004, arXiv:1602.04305.

[14] CMS Collaboration, "Constraints on anomalous Higgs boson couplings using production and decay information in the four-lepton final state", *Phys. Lett. B* **775** (2017) 1, doi:10.1016/j.physletb.2017.10.021, arXiv:1707.00541.

[15] CMS Collaboration, "Constraints on anomalous HVV couplings from the production of Higgs bosons decaying to τ lepton pairs", *Physical Review D* **100** (2019), no. 11, doi:10.1103/physrevd.100.112002, arXiv:1903.06973.

[16] ATLAS Collaboration, "Evidence for the spin-0 nature of the Higgs boson using ATLAS data", *Phys. Lett. B* **726** (2013) 120, doi:10.1016/j.physletb.2013.08.026, arXiv:1307.1432.

[17] ATLAS Collaboration, "Study of the spin and parity of the Higgs boson in diboson decays with the ATLAS detector", *Eur. Phys. J. C* **75** (2015) 476, doi:10.1140/epjc/s10052-015-3685-1, arXiv:1506.05669.

[18] ATLAS Collaboration, "Test of CP Invariance in vector-boson fusion production of the Higgs boson using the Optimal Observable method in the ditau decay channel with the ATLAS detector", *Eur. Phys. J. C* **76** (2016) 658, doi:10.1140/epjc/s10052-016-4499-5, arXiv:1602.04516.

[19] ATLAS Collaboration, "Measurement of inclusive and differential cross sections in the $H \to ZZ^* \to 4\ell$ decay channel in pp collisions at $\sqrt{s} = 13$ TeV with the ATLAS detector", *JHEP* **10** (2017) 132, doi:10.1007/JHEP10(2017)132, arXiv:1708.02810.

[20] ATLAS Collaboration, "Measurement of the Higgs boson coupling properties in the $H \to ZZ^* \to 4\ell$ decay channel at $\sqrt{s}$ = 13 TeV with the ATLAS detector", *JHEP* **03** (2018) 095, doi:10.1007/JHEP03(2018)095, arXiv:1712.02304.

[21] ATLAS Collaboration, "Measurements of Higgs boson properties in the diphoton decay channel with 36 fb^{-1} of pp collision data at $\sqrt{s} = 13$ TeV with the ATLAS detector", *Phys. Rev. D* **98** (2018) 052005, doi:10.1103/PhysRevD.98.052005, arXiv:1802.04146.

[22] C. Zhang and S. Willenbrock, "Effective-field-theory approach to top-quark production and decay", *Physical Review D* **83** (2011), no. 3, doi:10.1103/physrevd.83.034006, arXiv:1008.3869.

[23] R. Harnik et al., "Measuring CP violation in $h \to \tau^+\tau^-$ at colliders", *Physical Review D* **88** (2013), no. 7, doi:10.1103/physrevd.88.076009, arXiv:1308.1094.

[24] T. Ghosh, R. Godbole, and X. Tata, "Determining the spacetime structure of bottom-quark couplings to spin-zero particles", *Physical Review D* **100** (2019), no. 1, doi:10.1103/physrevd.100.015026, arXiv:1904.09895.

[25] A. V. Gritsan, R. Röntsch, M. Schulze, and M. Xiao, "Constraining anomalous Higgs boson couplings to the heavy-flavor fermions using matrix element techniques", *Physical Review D* **94** (2016), no. 5, doi:10.1103/physrevd.94.055023, arXiv:1606.03107.

[26] CMS Collaboration, "Measurements of $\mathrm{t\bar{t}H}$ production and the CP structure of the Yukawa interaction between the Higgs boson and top quark in the diphoton decay channel", (2020). arXiv:2003.10866. Submitted to *PRL*.

[27] ATLAS Collaboration, "Study of the CP properties of the interaction of the Higgs boson with top quarks using top quark associated production of the Higgs boson and its decay into two photons with the ATLAS detector at the LHC", (2020). arXiv:2004.04545. Submitted to *Phys. Rev. Lett.*

[28] D. Fontes, J. C. Romão, R. Santos, and J. P. Silva, "Large pseudoscalar Yukawa couplings in the complex 2HDM", *JHEP* **06** (2015) 060, doi:10.1007/JHEP06(2015)060, arXiv:1502.01720.

[29] S. King, M. Mühlleitner, R. Nevzorov, and K. Walz, "Exploring the CP-violating NMSSM: EDM constraints and phenomenology", *Nuclear Physics B* **901** (2015) 526, doi:10.1016/j.nuclphysb.2015.11.003, arXiv:1508.03255.

[30] S. Berge, W. Bernreuther, and S. Kirchner, "Determination of the Higgs CP-mixing angle in the tau decay channels at the LHC including the Drell–Yan background", *The European Physical Journal C* **74** (2014), no. 11, 3164, doi:10.1140/epjc/s10052-014-3164-0, arXiv:1408.0798.

[31] ATLAS Collaboration, "Probing the $\mathcal{CP}$ nature of the Higgs boson coupling to τ leptons at HL-LHC", Technical Report ATL-PHYS-PUB-2019-008, 2019.

[32] M. Krämer, J. Kühn, M. L. Stong, and P. M. Zerwas, "Prospects of measuring the parity of Higgs particles", *Zeitschrift für Physik C Particles and Fields* **64** (1994), no. 1, 21, doi:10.1007/bf01557231, arXiv:hep-ph/9404280.

[33] V. Barger et al., "Higgs bosons: Intermediate mass range at e+e- colliders", *Physical Review D* **49** (1994), no. 1, 79, doi:10.1103/physrevd.49.79, arXiv:hep-ph/9306270.

[34] J. R. Dell'Aquila and C. A. Nelson, "Distinguishing a spin-0 technipion and an elementary Higgs boson: V_1V_2 modes with decays into $\mathrm{l}_a^- \boldsymbol{l}_b$ and/or $\mathrm{q}_a^- \boldsymbol{q}_b$", *Phys. Rev. D* **33** (1986) 93, doi:10.1103/PhysRevD.33.93.

[35] K. Olive, "Review of particle physics", *Chinese Physics C* **40** (2016), no. 10, 100001, doi:10.1088/1674-1137/40/10/100001.

[36] S. Berge, W. Bernreuther, B. Niepelt, and H. Spiesberger, "How to pin down the CP quantum numbers of a Higgs boson in its τ decays at the LHC", *Physical Review D* **84** (2011), no. 11, doi:10.1103/physrevd.84.116003, arXiv:1108.0670.

[37] K. Desch, A. Imhof, Z. Was, and M. Worek, "Probing the CP nature of the Higgs boson at linear colliders with τ spin correlations; the case of mixed scalar-pseudoscalar couplings", *Physics Letters B* **579** (2004), no. 1-2, 157, doi:10.1016/j.physletb.2003.10.074, arXiv:0307.331.

[38] G. Bower, T. Pierzchala, Z. Was, and M. Worek, "Measuring the Higgs boson's parity using $\tau \to \rho\nu$", *Physics Letters B* **543** (2002), no. 3-4, 227, doi:10.1016/s0370-2693(02)02445-0, arXiv:hep-ph/0204292.

[39] CMS Collaboration, "The CMS trigger system", *JINST* **12** (2017) P01020, doi:10.1088/1748-0221/12/01/P01020, arXiv:1609.02366.

[40] CMS Collaboration, "The CMS experiment at the CERN LHC", *JINST* **3** (2008) S08004, doi:10.1088/1748-0221/3/08/S08004.

[41] P. Nason, "A new method for combining NLO QCD with shower Monte Carlo algorithms", *JHEP* **11** (2004) 040, doi:10.1088/1126-6708/2004/11/040, arXiv:hep-ph/0409146.

[42] S. Frixione, P. Nason, and C. Oleari, "Matching NLO QCD computations with parton shower simulations: the POWHEG method", *JHEP* **11** (2007) 070, doi:10.1088/1126-6708/2007/11/070, arXiv:0709.2092.

[43] S. Alioli, P. Nason, C. Oleari, and E. Re, "A general framework for implementing NLO calculations in shower Monte Carlo programs: the POWHEG BOX", *JHEP* **06** (2010) 043, doi:10.1007/JHEP06(2010)043, arXiv:1002.2581.

[44] S. Alioli et al., "Jet pair production in POWHEG", *JHEP* **04** (2011) 081, doi:10.1007/JHEP04(2011)081, arXiv:1012.3380.

[45] S. Alioli, P. Nason, C. Oleari, and E. Re, "NLO Higgs boson production via gluon fusion matched with shower in POWHEG", *JHEP* **04** (2009) 002, doi:10.1088/1126-6708/2009/04/002, arXiv:0812.0578.

[46] D. de Florian, G. Ferrera, M. Grazzini, and D. Tommasini, "Higgs boson production at the LHC: transverse momentum resummation effects in the $H \to \gamma\gamma$, $H \to WW \to l\nu l\nu$ and $H \to ZZ \to 4l$ decay modes", *Journal of High Energy Physics* **2012** (2012), no. 6, doi:10.1007/jhep06(2012)132, arXiv:1203.6321.

[47] M. Grazzini and H. Sargsyan, "Heavy-quark mass effects in Higgs boson production at the LHC", *Journal of High Energy Physics* **2013** (2013), no. 9, doi:10.1007/jhep09(2013)129, arXiv:1306.4581.

[48] T. Sjöstrand, S. Mrenna, and P. Z. Skands, "A Brief Introduction to PYTHIA 8.1", *Comput. Phys. Commun.* **178** (2008) 852, doi:10.1016/j.cpc.2008.01.036, arXiv:0710.3820.

[49] T. Sjöstrand et al., "An introduction to PYTHIA 8.2", *Comput. Phys. Commun.* **191** (2015) 159, doi:10.1016/j.cpc.2015.01.024, arXiv:1410.3012.

[50] T. Przedzinski, E. Richter-Was, and Z. Was, "Documentation of *TauSpinner* algorithms: program for simulating spin effects in τ -lepton production at LHC", *Eur. Phys. J. C* **79** (2019), no. 2, 91, doi:10.1140/epjc/s10052-018-6527-0, arXiv:1802.05459.

[51] J. Alwall et al., "The automated computation of tree-level and next-to-leading order differential cross sections, and their matching to parton shower simulations", *JHEP* **07** (2014) 079, doi:10.1007/JHEP07(2014)079, arXiv:1405.0301.

[52] J. Alwall et al., "Comparative study of various algorithms for the merging of parton showers and matrix elements in hadronic collisions", *Eur. Phys. J. C* **53** (2008) 473, doi:10.1140/epjc/s10052-007-0490-5, arXiv:0706.2569.

[53] CMS Collaboration, "Event generator tunes obtained from underlying event and multiparton scattering measurements", *Eur. Phys. J. C* **76** (2016) 155, doi:10.1140/epjc/s10052-016-3988-x, arXiv:1512.00815.

[54] GEANT4 Collaboration, "GEANT4—a simulation toolkit", *Nucl. Instrum. Meth. A* **506** (2003) 250, doi:10.1016/S0168-9002(03)01368-8.

[55] CMS Collaboration, "Particle-flow reconstruction and global event description with the CMS detector", *JINST* **12** (2017), no. 10, P10003, doi:10.1088/1748-0221/12/10/P10003, arXiv:1706.04965.

[56] CMS Collaboration, "Performance of CMS muon reconstruction in pp collision events at $\sqrt{s} = 7$ TeV", *JINST* **7** (2012) P10002, doi:10.1088/1748-0221/7/10/P10002, arXiv:1206.4071.

[57] CMS Collaboration, "Performance of electron reconstruction and selection with the CMS detector in proton-proton collisions at $\sqrt{s} = 8$ TeV", *JINST* **10** (2015) P06005, doi:10.1088/1748-0221/10/06/P06005, arXiv:1502.02701.

[58] M. Cacciari, G. P. Salam, and G. Soyez, "The anti-k_t jet clustering algorithm", *JHEP* **04** (2008) 063, doi:10.1088/1126-6708/2008/04/063, arXiv:0802.1189.

[59] CMS Collaboration, "Jet algorithms performance in 13 TeV data", CMS Physics Analysis Summary CMS-PAS-JME-16-003, 2017.

[60] CMS Collaboration, "Identification of heavy-flavour jets with the CMS detector in pp collisions at 13 TeV", *Journal of Instrumentation* **13** (2018), no. 05, P05011, doi:10.1088/1748-0221/13/05/p05011, arXiv:1712.07158.

[61] CMS Collaboration, "Performance of missing transverse momentum in pp collisions at $\sqrt{s} = 13$ TeV using the CMS detector", CMS Physics Analysis Summary CMS-PAS-JME-17-001, 2018.

[62] CMS Collaboration, "Performance of reconstruction and identification of τ leptons decaying to hadrons and ν_τ in pp collisions at $\sqrt{s} = 13$ TeV", *Journal of Instrumentation* **13** (2018), no. 10, P10005, doi:10.1088/1748-0221/13/10/p10005, arXiv:1809.02816.

[63] CMS Collaboration, "Performance of the DeepTau algorithm for the discrimination of taus against jets, electron, and muons", CMS Detector Performance Note CMS-DP-2019-033, 2019.

[64] T. Chen and C. Guestrin, "Xgboost: A scalable tree boosting system", in *Proceedings of the 22nd ACM SIGKDD International Conference on Knowledge Discovery and Data Mining*, KDD '16, p. 785. Association for Computing Machinery, New York, NY, USA, 2016. arXiv:1603.02754. doi:10.1145/2939672.2939785.

[65] CMS Collaboration, "Description and performance of track and primary-vertex reconstruction with the CMS tracker", *JINST* **9** (2014) P10009, doi:10.1088/1748-0221/9/10/P10009, arXiv:1405.6569.

[66] K. Rose, "Deterministic annealing for clustering, compression, classification, regression, and related optimization problems", *Proceedings of the IEEE* **86** (1998), no. 11, 2210.

[67] W. Waltenberger, R. Frühwirth, and P. Vanlaer, "Adaptive vertex fitting", *Journal of Physics G: Nuclear and Particle Physics* **34** (2007), no. 12, N343, doi:10.1088/0954-3899/34/12/n01.

[68] CMS Collaboration, "An embedding technique to determine $\tau\tau$ backgrounds in proton-proton collision data", *Journal of Instrumentation* **14** (2019), no. 06, P06032, doi:10.1088/1748-0221/14/06/p06032, arXiv:1903.01216.

[69] CMS Collaboration, "Measurement of the $Z\gamma^* \to \tau\tau$ cross section in pp collisions at $\sqrt{s} = 13$ TeV and validation of τ lepton analysis techniques", *Eur. Phys. J. C* **78** (2018), no. 9, 708, doi:10.1140/epjc/s10052-018-6146-9, arXiv:1801.03535.

[70] CMS Collaboration, "Measurements of inclusive W and Z cross sections in pp collisions at $\sqrt{s} = 7$ TeV", *Journal of High Energy Physics* **2011** (2011), no. 1, doi:10.1007/jhep01(2011)080, arXiv:1012.2466.

[71] CMS Collaboration, "Determination of jet energy calibration and transverse momentum resolution in CMS", *Journal of Instrumentation* **6** (2011), no. 11, 11002, doi:10.1088/1748-0221/6/11/p11002, arXiv:1107.4277.

[72] CMS Collaboration, "Measurement of the differential cross section for top quark pair production in pp collisions at $\sqrt{s} = 8$ TeV", *The European Physical Journal C* **75** (2015), no. 11, doi:10.1140/epjc/s10052-015-3709-x, arXiv:1505.04480.

[73] CMS Collaboration, "Measurement of Higgs boson production and decay to the $\tau\tau$ final state", CMS Physics Analysis Summary CMS-PAS-HIG-18-032, 2019.

[74] S. Berge, W. Bernreuther, and S. Kirchner, "Prospects of constraining the Higgs boson's CP nature in the tau decay channel at the LHC", *Physical Review D* **92** (2015), no. 9, doi:10.1103/physrevd.92.096012, arXiv:1510.03850.

[75] CMS Collaboration, "CMS Luminosity Measurements for the 2016 Data Taking Period", CMS Physics Analysis Summary CMS-PAS-LUM-17-001, 2017.

[76] CMS Collaboration, "CMS luminosity measurement for the 2017 data-taking period at $\sqrt{s} = 13$ TeV", CMS Physics Analysis Summary CMS-PAS-LUM-17-004, 2018.

[77] CMS Collaboration, "CMS luminosity measurement for the 2018 data-taking period at $\sqrt{s} = 13$ TeV", CMS Physics Analysis Summary CMS-PAS-LUM-18-002, CERN, 2019.

[78] Y. Li and F. Petriello, "Combining QCD and electroweak corrections to dilepton production in the framework of the FEWZ simulation code", *Physical Review D* **86** (2012), no. 9, doi:10.1103/physrevd.86.094034, arXiv:1208.5967.

[79] M. Czakon and A. Mitov, "Top++: A program for the calculation of the top-pair cross-section at hadron colliders", *Computer Physics Communications* **185** (2014), no. 11, 2930, doi:10.1016/j.cpc.2014.06.021, arXiv:1112.5675.

[80] CMS Collaboration, "Measurement of the WZ production cross section in pp collisions at $\sqrt{s} = 13$ TeV", *Physics Letters B* **766** (2017) 268, doi:10.1016/j.physletb.2017.01.011, arXiv:1607.06943.

[81] CMS Collaboration, "Cross section measurement of t-channel single top quark production in pp collisions at $\sqrt{s} = 13$ TeV", *Physics Letters B* **772** (2017) 752, doi:10.1016/j.physletb.2017.07.047, arXiv:1610.00678.

[82] LHC Higgs Cross Section Working Group, "Handbook of LHC Higgs cross sections: 4. deciphering the nature of the Higgs sector", *CERN* (2016) doi:10.23731/CYRM-2017-002, arXiv:1610.07922.

[83] R. Barlow and C. Beeston, "Fitting using finite monte carlo samples", *Computer Physics Communications* **77** (1993) 219, doi:10.1016/0010-4655(93)90005-W.

[84] J. S. Conway, "Incorporating Nuisance Parameters in Likelihoods for Multisource Spectra", (2011). arXiv:1103.0354. To be published in a CERN Yellow Report.

[85] The ATLAS Collaboration, The CMS Collaboration, The LHC Higgs Combination Group, "Procedure for the LHC Higgs boson search combination in Summer 2011", Technical Report CMS-NOTE-2011-005, ATL-PHYS-PUB-2011-11, 2011.

[86] CMS Collaboration, "Precise determination of the mass of the Higgs boson and tests of compatibility of its couplings with the standard model predictions using proton collisions at 7 and 8 TeV", *Eur. Phys. J. C* **75** (2015) 212, doi:10.1140/epjc/s10052-015-3351-7, arXiv:1412.8662.